UNIVERSITY OF OKLAHOMA

GRADUATE COLLEGE

METHOD OF REHABILITATION FOR CORROSION DAMAGE
IN THE END REGION OF PRESTRESSED CONCRETE BRIDGE GIRDERS

A THESIS

SUBMITTED TO THE GRADUATE FACULTY

in partial fulfillment of the requirements for the degree of

MASTER OF SCIENCE

By

MINH PHUOC HUYNH
Norman, Oklahoma
2021

METHOD OF REHABILITATION FOR CORROSION DAMAGE
IN THE END REGION OF PRESTRESSED CONCRETE BRIDGE GIRDERS

A THESIS APPROVED FOR THE SCHOOL OF CIVIL ENGINEERING AND
ENVIRONMENTAL SCIENCE

BY THE COMMITTEE CONSISTING OF

Dr. Royce W. Floyd, Chair

Dr. Jeffery S. Volz

Dr. Jin-Song Pei

I would like to dedicate this thesis to my grandparents, parents and my wife for their

unconditional love, inspiration, support, passion, and believe in me.

Acknowledgement

First and foremost, I would like to extend my heartfelt thanks and deepest appreciation to my advisor, Dr. Royce Floyd, for his unconditional support, patience, guidance, and confidence in me to complete this research. I am also grateful to Dr. Jeffery Volz and Dr. Jin-Song Pei for providing guidance and advice to improve the thesis as committee members.

I would like to thank the team of undergraduate, graduate researchers, and Fears Lab faculty that supported and helped me completing my thesis. Especially, a great thanks to Mike Schmitz, Trevor Looney, Jacob Choate, Stephen Roswurm, Mujtaba Ahmadi, Kim Serey Vuth Chea, Michael Mesigh, Kevin Lepissier, Dip Banik, Cade Harris, John Guerrero, and Cole Walker for helping me build and test the specimens throughout the research. I would like to thank ODOT for funding this project, and Dolese Bros. Co. for donating materials.

Last, I would like to thank my friends and my family for spiritual support through this period. I would not complete and be here today without their love, understanding, and motivation.

Table of Contents

List of Tables

List of Figures

Chapter 1 Introduction

1.1 Background

Bridges are indispensable parts of a transportation system. They connect two roads, two sides of a river, and even between islands and the mainland. However, a study conducted by ASCE (the American Society of Civil Engineers) in 2017 classified only "C+" for the U.S bridges' condition. Within the report, there were 614,387 bridges in service around the U.S, and almost 40% of them were built 50 years ago or more. Most of these bridges have a typical design life of 50 years. Also, 56,001 bridges (9.1%) were classified as "structurally deficient" in 2016. The report noted that the number of structurally deficient bridges had decreased gradually since previous decades, but many bridges were approaching the end of their design lives (Infrastructure Report Card, 2017).

In 2018, the U.S Department of Transportation released a detailed table reporting the number of bridges based on their conditions. There were 616,096 bridges in total, but 47,054 bridges (7.6%) were listed in poor condition or "structural deficient" (Federal Highway Administration, Bridge Condition by Highway System 2018, 2018). The condition of these bridges comes from gaining damage during their service life. For prestressed concrete bridges, natural and man-made hazards, which come from accidents, construction, design flaws and manufacturing errors, can lead to damage to bridges. Weather and chemical corrosion are some of the most common sources of damage and deteriorate the concrete over time. This reaction continues until the protective concrete layers for the internal reinforcement are worn away. Once the protective layers are removed from the internal reinforcement the corrosion rate accelerates. Consequently, the capacity of a concrete member shall be reduced due to the loss of steel

reinforcement area to corrosion. This is a common cause of deterioration of concrete structures (Guettala & Abibsi, 2006).

According to the Federal Highway Administration (FHWA), the number of prestressed concrete bridges in service increases annually, which shall overcome the number of the steel bridges and reinforced concrete bridges built since the 1970s (Federal Highway Administration, 2013). Prestressed concrete bridges are more common in construction due to their advantages such as low cost, required maintenance, time, and quality control. However, as introduced above, concrete bridges have some disadvantages and are susceptible to corrosion at the end regions.

Moreover, prestressed concrete girders have an anchorage zone in the end region, where the prestress force is transferred from the prestressing strands to the concrete, and in that region the prestress is not fully developed to resist the shear load or other external loads. The end region of the concrete bridges is also often directly beneath deck joints which often leak water containing deicing chemicals from the surface of a bridge onto its girders. This chemically laden water leads to corrosion and eventually spalling of the girder ends. In previous research, deterioration was observed in all prestressed concrete girders examined, but corrosion damage was only observed at the girder ends (Mayhorn, 2016). Therefore, there is a need to rehabilitate the end regions of prestressed bridges in service using different types of concrete materials without stopping traffic.

1.2 Objectives

The goal of this research is to expand the body of knowledge surrounding repair of deterioration caused by corrosion in the end zone of prestressed concrete girders due to natural

2

and human hazards. To rehabilitate the corroded end region, three innovative concrete materials: FR-SCC, UHPC, and MALP were examined. After reviewing current available literature, three objectives were identified.

- Conduct experimental repair and retrofitting of prestressed concrete girders with simulated corrosion damage in the end regions, which interferes with the prestressing strand bond and causes a reduced prestress force at the end region.

- Evaluate cracking resistance, bonding between the conventional concrete and repair, and contribution of thin UHPC, FR-SCC, and MALP concrete repairs to structural strength.

- Create guidance for designing repairs of prestressed concrete girders using UHPC, FR-SCC, and MALP concrete materials, including mixing, placement, and quality control for use in Oklahoma bridge repair.

Chapter 2 Literature Review

2.1 Prestressed Concrete and Corrosion

In 1888, the concept of prestressed concrete first appeared as prestressed concrete design was first patented by P.H. Jackson. However, the technology of constructing prestressed concrete was limited until Eugene Freyssinet defined the need for high strength steel with low relaxation for use as a structural building material. After World War II, prestressed concrete was applied generally in Europe to reconstruct infrastructure. In 1949, the Walnut Lane Bridge in Philadelphia was constructed using prestressed concrete technology by a Belgian engineer, Gustave Magnel, which was the first prestressed concrete bridge in the United States and revolutionized the construction industry in America (Dinges, 2009). Prestressed concrete bridges were a desirable alternative to steel and reinforced concrete construction with advantages of cost, labor, efficiency, and maintenance (Yee, 1976). In a prestressed concrete girder, the end region plays a significant role in the overall function of the girder design. For prestressed concrete technology, high strength steel reinforcement with low relaxation is tensioned before casting concrete (for pre-tensioning) or after casting concrete (for post-tensioning). Then, in pre-tensioned elements the strand is cut (at release) to transfer the prestressing forces to the member through the bond between strands and concrete in the beam. In post-tensioned elements the prestress force is transferred to the beam at the time of prestressing through the use of end anchorages. The region where prestressing forces are transferred to the beam in a pre-tensioned element, is called prestress transfer zone or the force distribution region at the end of the beam. This region requires a higher concentration of mild steel reinforcement than other regions in order to resist potential transverse cracking in the end region caused by the concentrated prestress forces. The girder end region with the high percentage of steel reinforcement is often

directly underneath a bridge deck joint that may leak and create a path for water and chlorides from deicing salts to reach the girder ends. The end of the girder then becomes more susceptible to reinforcement corrosion and concrete spalling, which could lead to reduced capacity and ultimate structural collapse. As vehicles drive over a bridge, they act as moving point loads along the girders which combine with the dead loads of the girders and bridge deck to cause shear forces at the end of the girder. These large shear forces can contribute to end region deterioration due to the loss of strength in concrete, mild steel reinforcement, and prestressing strands caused by corrosion.

A study was conducted to investigate 19 representative prestressed concrete bridges in the state of Oklahoma (Mayhorn, 2016). Deterioration was observed in all cases, but corrosion damage was only observed at the girder ends (Mayhorn, 2016). As mentioned above, the corroded end regions have the potential to lead to loss of capacity, which can cause catastrophic failure if the girder is not replaced or repaired properly. However, replacing with a new girder has significant costs in the form of money, time, and labor, even not counting traffic disruption during construction. This is evidence to justify applying new concrete materials to rehabilitate old or damaged girders to restore the original strength capacity and to protect the end regions from additional corrosion.

Another study was conducted by Abosraa et al. (2011) to examine the effect of different compressive strengths on the corrosion of steel bars embedded in concrete cubes. Part of this study monitored samples of specimens with different compressive strengths after exposure to a chloride solution for 1, 7 and 15 days to compare how specimens were corroded after each period of days. Macroscopic observation indicated the embedded steel bar was severely corroded with deep pitting when exposed to chloride solution for up to 15 days. The researchers concluded

that the corrosion rate of steel bars increased based on the extension of the accelerated corrosion time and the increase in corrosion rate decreased the concrete and bond strength (Abosraa et al., 2011). Bruce et al. (2008) concluded that corrosion of prestressing strands reduces the structural performance of a beam faster than corrosion in conventional reinforcement because of the loss of a greater proportion of the steel cross-section due to the small area and high stresses in prestressed reinforcement. Szilar (1969) also emphasized that prestressing steel was subjected to significantly higher stresses with smaller diameters in relation to conventional reinforcement.

2.2 Ultra-High Performance Concrete (UHPC)

Ultra-high performance concrete (UHPC) is a relatively recent new class of cementitious composites with many advantages for the construction industry through advancements in the materials science. The outstanding mechanical properties of this material furnish the performance that significantly exceeds that of conventional concrete.

According to the U.S. Department of Transportation Federal Highway Administration (FHWA), UHPC is defined as "a cementitious composite material composed of an optimized gradation of granular constituents, a water-to-cementitious material ratio less than 0.25, and high percentage of discontinuous internal fiber reinforcement" (Graybeal B. A., 2011). UHPC has an extremely low porosity due to the optimized particle gradation, low water-cementitious materials ratio facilitated through the use of superplasticizer and use of silica fume. Additionally, the presence of very fine quartz instead of ordinary coarse aggregate helps the UHPC have better microstructure and performance (Kusumawardaningsih et al., 2015). As a result, UHPC exhibits very high compressive strength of more than 18.3 ksi with untreated curing. In addition, the

tensile strength of UHPC, both before and after tensile cracking, is higher than for conventional concrete (Graybeal B. A., 2006). According to the FHWA definition presented by (Graybeal B. A., 2011), UHPC has a compressive strength that reaches over 21.7 ksi (150 MPa) and a post-cracking tensile strength greater than 0.72 ksi (5 MPa). As a result, the mechanical properties of UPHC have the potential for advantage in use for highway infrastructure deterioration replacement and repair (Graybeal B. A., 2014).

As UHPC has not been widely used as a repair material for bridge girders, a study evaluated the effectiveness of applying UHPC to repair damaged girder joints by retrofitting cracked joints between girders made continuous for live load (Mesigh, 2021). This research focused on testing flexural behavior, in both positive and negative bending moment, of repaired joints compared to the control joints which were tested at the beginning. The positive and negative flexural capacities of the repaired continuity joints were fully restored after rehabilitation. Mesigh (2021) recommended using UHPC for repairing joints for its advantage of having little or no cracking on the repaired surfaces even after significant loading resulting in protection of internal steel reinforcement against weather exposure. Ahmadi (2021) conducted research focused on applying UHPC as a repair material for shear failure at the end regions of bridge girders at the University of Oklahoma. For that research, the thin layer of UHPC was placed around the end region where the failure occurred out to the loading point, which was 3.5 ft from the end of the girder. Then, the repaired beam was reloaded until failure to verify how the repair material contributed to restore the loss of shear capacity. The result pointed out that UHPC over performed in increasing the shear capacity more than the original beam with the smallest repair thickness (Ahmadi, 2021). Zmetra (2015) conducted an experiment to test both undamaged and damaged steel girders to failure and to examine the effectiveness of a UHPC

7

repair. One damaged girder was retrofitted with UHPC and retested after 28 days. The results indicated that UHPC provided enough bracing to eliminate a web buckling failure and ensured a yield failure. Therefore, the UHPC could enhance the end region capacity of steel bridge girders.

2.3 Fiber-Reinforced Self-Consolidating Concrete (FR-SCC)

Another material with significant potential for bridge girder repair and rehabilitation is Fiber reinforced self-consolidating concrete (FR-SCC). Since self-consolidating concrete (SCC) was invented in Japan in 1989, it has been used globally in the construction industry. It brings many advantages not only to construction firms, but also clients and communities. Myint Lwin, Director of the Federal Highway Administration's (FHWA) Office of Bridge Technology, summarized: "Whatever conventional concrete can do, SCC can do better, faster and cheaper, especially for concrete elements with special textures, complex shapes, and congested reinforcement" (Federal Highway Administration, 2005). SCC mixes have a high degree of workability or flowability and are stable during and after placement. It has an ability to flow into and completely fill intricate and complex forms, to pass through and bond to congested reinforcement material, and to consolidate under its own weight (gravity). It also has high resistance to aggregate segregation (Federal Highway Administration, 2005).

Fibers are small reinforcement with various geometries, length, materials, and sizes often added to cementitious materials (concrete, mortar, and grout) to improve performance in various applications. Because fibers are individually separate and distinct and distribute throughout the concrete, they can be used to control cracking due to plastic shrinkage and improve the resistance to flexure, fatigue, impact, and pull-out where the fibers' role is bridging cracks and increasing

stiffness (Kassimi, 2013). Kassimi (2013) conducted a study of the performance and development of FR-SCC by mixing FR-SCC mixes with different percentages of fibers having various geometries and comparing performance to conventional concrete. As a result, the researcher concluded that FR-SCC exhibited better durability performance than conventional concrete in terms of chloride ion permeability and capillary porosity, which were reduced up to 90% and 25%, respectively. Moreover, fibers could replace 50% of steel reinforcement in the tension repair zone without reducing the structural performance (Kassimi, 2013).

Several other research projects have been conducted on FR-SCC for structural repairs at the University of Oklahoma. Wirkman (2016) investigated the application of FR-SCC in retrofitting the tension zone of small-scale and full-scale beams. His research was performed by testing two sets of beams with different percentages of Type-K shrinkage-compensating cement and comparing with a set of control beams using an ODOT Class AA concrete mix. For material properties testing, he confirmed that FR-SCC was qualified for repair application with advantage of good compaction without requiring vibration or exhibiting segregation and blockage. From the full-scale testing, Wirkman (2016) concluded that the two repaired beam sets "were statistically equivalent to the control beams". In addition, Choate (2018) researched the application of FR-SCC in repairing prestressed girders. His study was conducted by taking a 46-year-old conventional concrete AASHTO Type II prestressed bridge girder that had previously been loaded until failure at both ends. Then, the girder ends were repaired using FR-SCC. Damaged concrete was removed, and one end was post-tensioned to restore the prestressing force. At an age of 28 days after casting the FR-SCC repair, the Type II prestressed girder was re-tested in order to examine the strength of the repaired girder compared to the original girder's

strength. In conclusion, Choate (2018) confirmed that 80% of the original strength of the girder was recovered.

2.4 Magnesium-Alumino-Liquid Phosphate Concrete (MALP)

Magnesium-Alumino-Liquid Phosphate (MALP) concrete is a fast-setting concrete material with potential for excellent bond with base concrete and corrosion resistance, which both are potentially beneficial for beam end repairs, especially where speed of repair is a consideration. According to Phoscrete's official website, their product incorporates a pre-packaged magnesium alumina-aggregate dry powder (including magnesium, calcined aluminosilicates, graded aggregate, and fibers) and a mono-aluminum-liquid phosphate activator. Based on the manufacturer's data, the advantages of Phoscrete compared to the conventional concrete are labor and time savings, easy and accurate mixing (two components: dry mix in a bag and liquid activator in a jug compared to many components in conventional concrete), rapid return to service (traffic-ready in 30 minutes), high chloride resistance, no shrinkage and cracking, no need for curing, and use in all temperatures (can be set in temperature cold as -5°F). It also does not require any water or prewetting of the concrete surface. Because of the rapid strength gain and quick-setting properties, Phoscrete could become a high value resource for concrete repair. The physical properties of Phoscrete MALP concrete determined by ASTM standard testing procedure indicate that it can achieve 5,000 psi in one hour and 11,500 psi in 28 days based on ASTM C109, and flexural strength modulus of rupture of 500 psi in one day and 700 psi in 28 days based on ASTM C78 (Phoscrete, 2021). According to Fourier (2014), MALP technology was initially developed to patch concrete floors and other surfaces which were exposed to high-temperature spills and other punishing industrial activities. MALP concrete was

introduced to transportation agencies as an alternative technology to repair spalled concrete bridge decks, expansion joint nosing, and beams (Floyd et al., 2021). However, limited information is available on the performance of Phoscrete and MALP concrete in general, which will inhibit the uses of Phoscrete and other MALP concrete products in practice.

2.5 Bond-Loss Failure Mechanism

In actual situations, girders can fail for many reasons. Often girders are designed with flexure as the controlling failure mechanism, but especially for girders with end region damage, other failure mechanisms may control. One typical failure type for prestressed girder end regions is a bond-loss failure. This type of failure has been examined extensively in previous research, but Naji et al. (2016) summarized previous research and examined failures that had shear occurring near the support with the objective of providing a standardized classification of bond-loss failures. In this research, bond-loss failures were divided into multiple subcategories with behaviors and cracking patterns as described in Figure 2.1. Also, the label for each category had two parts in the following format: primary failure mode – secondary or contributing failure mode (Naji et al., 2016). In general, there are four types of bond-loss failures: bond-shear, bond-flexure, flexure-bond, and bond-shear/flexure. Each type is distinguished in the summary below and described in Figure 2.1, which contains drawings of the cracking pattern and graphs of load vs. deflection and strand slip.

a) *Bond-shear failure:* For this type of failure the primary inclined cracks initiate in the web and bottom flange near the support, in which they disturb anchorage of the strands and lead to a loss of strand to concrete bond and strand slipping. A bond-shear failure

may occur at lower load than a typical shear failure. Most of the observed bond-shear failures in the research occurred at shear span-to-depth ratios (a/d) less than 3.

b) *Bond-flexure failure:* For this failure type, the initial cracks do not necessarily cause strand slip. Nevertheless, the girders lose stiffness and load-deflection response becomes nonlinear after cracking. As the cracks intercept the prestressing strands in the end region, bond loss and strand slip start occurring. Strand slip causes cracks to open wider and increase the flexural strain. The peak load corresponds with crushing of the top flange or deck and is less than that associated with the nominal flexural capacity. The shear span-to-depth ratio associated with this failure type is greater than 2.5.

c) *Flexure-bond failure:* This type of failure is similar to a typical flexural failure with a small degree of strand slip observed near peak load. The load – deflection response of this failure is ductile, and the peak load occurs at the same time as the compression flange starts crushing. Bond-loss and strand slip are only noticed near the load which crushes the concrete flange. The shear span-to-depth ratio resulting in a flexure-bond failure is greater than 2.5.

d) *Bond-shear/flexure failure:* This is a hybrid failure mode where bond loss is the primary cause for failure, but both shear and flexural failures occur as a result of bond loss and strand slip. The initial inclined cracks and/or flexural cracks form in the web and bottom flange near the support. The combination of shear and flexure acting on the compression zone leads to crushing of the flange at peak load. The shear span-to-depth ratio associated with bond-shear/flexure failure is 2.5 or less.
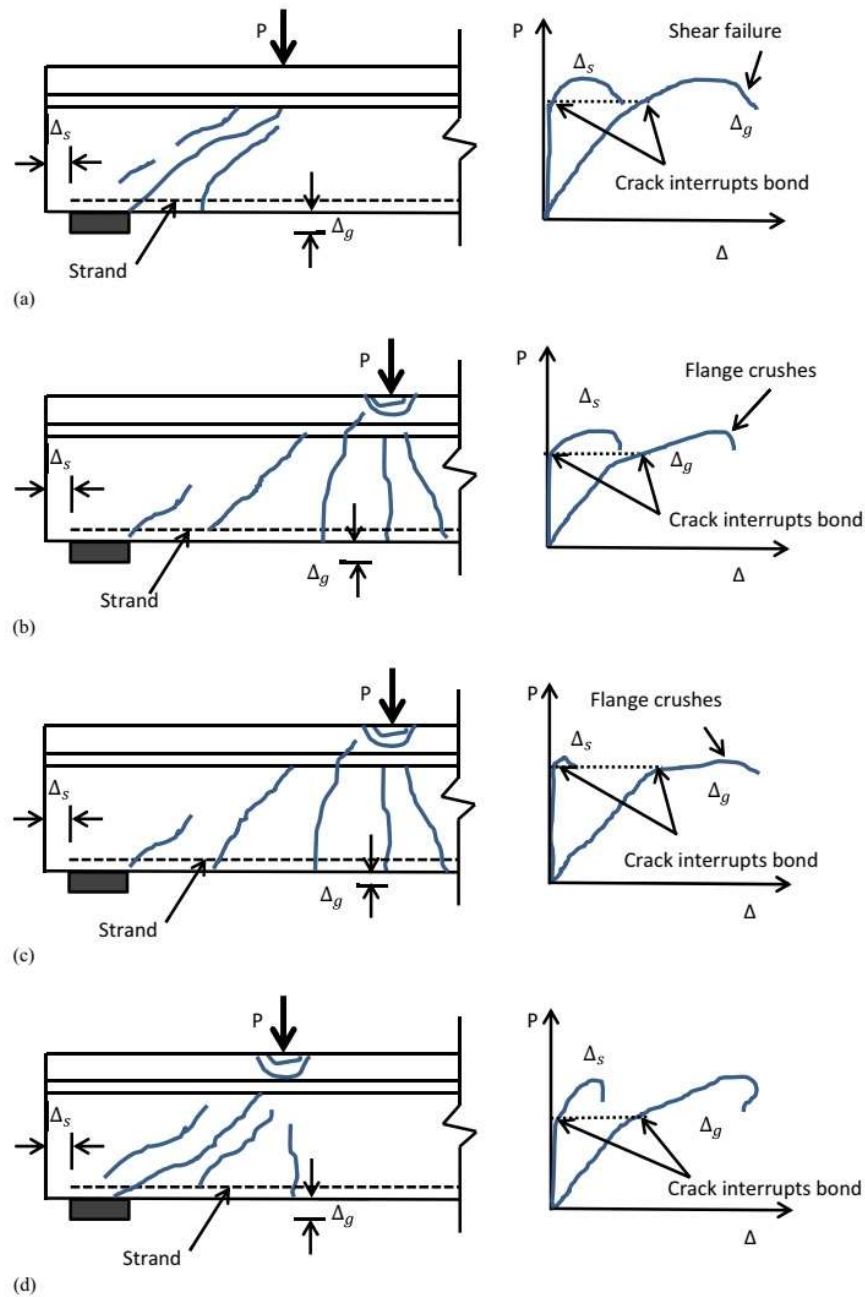
Figure 2.1: Typical Crack Pattern and Load-Deflection Behavior for: a) bond-shear; b) bond-flexure; c) flexure-bond; d) bond-shear/flexure failures (Naji et al., 2016)

The failure mechanisms described in Naji's research help to distinguish the failure mode of prestressed concrete girders using a point load with measured deflection and strand slip. This

allows a more objective measure of comparison between beam tests. Naji's research also helps to ensure the accuracy of computed capacity for the girder and determine locations where bond loss reduces the strength of the girder.

2.6 Summary

More bridges will become deficient year after year, and prestressed concrete bridge girder end regions are a potential source of deterioration contributing to these deficiencies. The end region is where supports are located and contributes to load transfer to the bridge substructure. Issues occurring at the end region could lead to failure of the girders and the entire bridge structure. Therefore, solutions for rehabilitating corroded end regions are necessary to extend the life of existing bridges. Using conventional concrete for repair is an option but may not be the optimal choice. Innovative concrete materials such as FR-SCC, UHPC, and MALP are considered to be potential solutions for rehabilitation because of their advantages such as excellent workability, rapid hardening, and high durability. However, little information is available on the structural performance of girder end regions repaired with these materials. The research described in this thesis examined application of these materials for repair of girders with simulated corrosion induced damage and to examine potential quality-control testing methods for each repair material, information that was missing from the literature.

Chapter 3 Methods and Approach

3.1 Overview

In this chapter, the methods of constructing the girder specimens and procedures used for experimental testing are described and discussed. During this research, nine 18 ft-long girders scaled to be approximately half size AASHTO Type II girders were constructed with induced damage, repaired, and tested. They were constructed using self-consolidating concrete (SCC) for the girders themselves and ODOT Class AA concrete for their deck sections. The repairs were constructed with UHPC, FR-SCC, and MALP concrete. In order to apply new concrete materials to existing concrete in the bridge girders, the bond behavior of the new material to the existing concrete should first be understood. A splitting tensile strength test (ASTM C496) and a slant shear test (ASTM C882) were conducted to determine how effectively each type of concrete repair material bonds to the base concrete. To examine the structural performance of the repairs, prestressed girders were then built with a hollow space at the bottom of the end region of each girder with dimensions of 18 in. x 9 in. x 2 in. to simulate a corrosion region where concrete spalling occurs. Those hollow spaces were filled with the concrete repair materials at least 28 days after the placement of the conventional concrete for the girders. After the repair materials had reached an age of 28 days, the girders were loaded to failure using a hydraulic system to perform an experimental shear test. The results shall quantify the efficiency of the new materials for end region corrosion repair purposes.

3.2 Prestressed Girder Design, Construction, and Testing

3.2.1 Prestressed Girder Design

The prestressed girder specimen used for this research was designed based on selecting desired geometry, location and number of prestressing strands used, shear reinforcement and concrete mix design. All of the design and construction steps were conducted at Donald G. Fears Structural Engineering Laboratory. The geometry of the girder was selected as an approximately half-scale AASHTO Type II girder with a length of 18 ft used in previous research projects at the University of Oklahoma (Mayhorn, 2016 and Mesigh 2021). The prestressing strand type was selected to be 0.5 in. special Grade 270 low-relaxation strand based on material availability. The prestressing strands were spaced 2 in. center to center and placed 2 in. from the bottom of the girder to center of the strands. A value of 2 in. from the bottom of the flange would provide the minimum concrete cover while maximizing the compression stress and moment capacity. Also, it matched the design from the previous research done at the University of Oklahoma. During the design process, stresses at the midspan of the girder's top exceeded the tension limits given by ACI 318-14 Section 24.5.3 at prestress release. To counter the tension force and meet the code requirements, two additional No. 5 Grade 60 reinforcing bars were placed 2.465 in. from the top of the girder's deck. For shear reinforcement, double No. 3 C-shaped stirrups were used along the girder with four different stirrup spacing intervals based on shear capacity calculation in Chapter 7 Section 7.3 with extra projection at the top of the girder to create composite action with the concrete deck as shown in Figures 3.1 and 3.2.
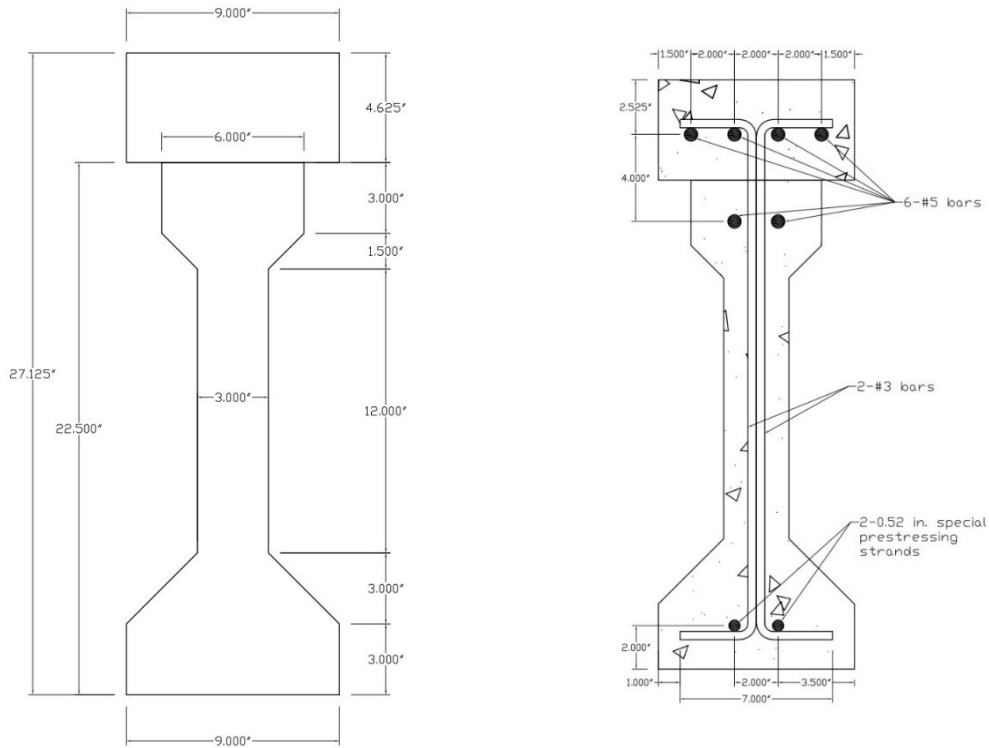
Figure 3.1: Girder Dimensions (Left) and Stirrup Dimensions (Right)
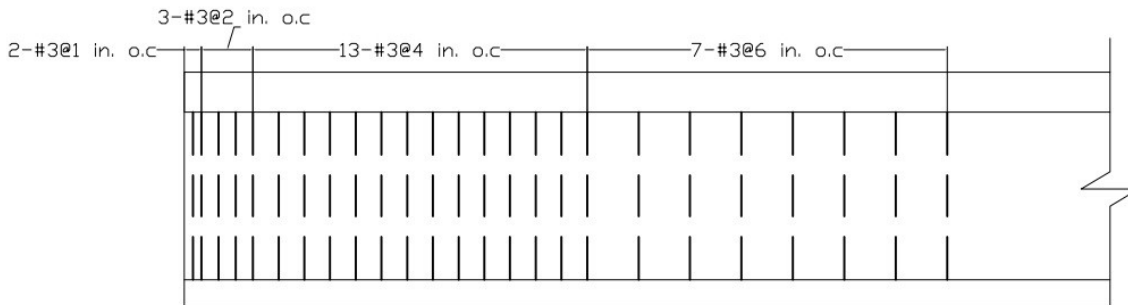
Figure 3.2: Stirrup Distribution in Girder

The SCC mix design used for the beams was developed from previous research at OU
(Mayhorn, 2016), with adjustments to satisfy the requirements for specific conditions such as
temperature, materials, and moisture. The minimum requirement for compressive strength at 24

hours was 4000 psi for prestress release and 7000 psi was targeted after 28 days. The slump flow test (ASTM C1611) was conducted immediately after blending all constituent materials in order to determine the workability of the self-consolidating concrete. A range of 22.0 in to 28.0 in. was targeted for the flow test. Table 1 lists the material proportions for the final mix design.

Table 3.1: Material Proportion of Self-Consolidating Concrete used for Girder Construction

Material Portion	Quantity
Portland Type (I/II) Cement (lb/yd^3)	851
Coarse Aggregate (lb/yd^3)	1364
Fine Aggregate (lb/yd^3)	1472
Water (lb/yd^3)	310
Glenium 7920 (HRWR) (oz/cwt)	9

The material portion includes Glenium 7920, which is a commonly used high range water reducing admixture. This admixture is added to the mix to reduced required mixing water and produce great flowability while increasing concrete strength, decreasing drying shrinkage, and enhancing concrete bond strength. The unit of Glenium 7920 is oz/cwt that stands for fluid ounces per hundredweight of cement. This unit means for every 100 pounds of the combined cementitious materials (e.g., cement, silica fume, Komponent, fly ash, etc.), one ounce of HRWR was used. The coarse aggregate was 3/8 in. limestone aggregate and the fine sand used for mixing was washed concrete sand. Table 3.1 is based on the saturated surface dry condition for the coarse aggregate and sand.

3.2.2 Prestressed Girder Construction

The construction process for each prestressed girder involved two main activities: set up and casting. The girder set up process started with cutting and bending the shear stirrups. The stirrups were next tied to the top steel reinforcing bars at the required spacings shown in Figure 3.2 to create a reinforcement cage. The next step was to set up, level and oil the prestressing bed in order to prevent concrete hardening on the bed during settlement. One of the steel formwork sides was put into place on the prestressing bed and the reinforcement cage was placed on the prestressing bed and attached to the steel beam form on one side. An 18 in. x 9 in. x 2 in. foam block, in which 0.5 in. deep trenches to cover half of the strands were created, was placed at one end of the girder to represent the corroded region, as shown in Figure 3.3.
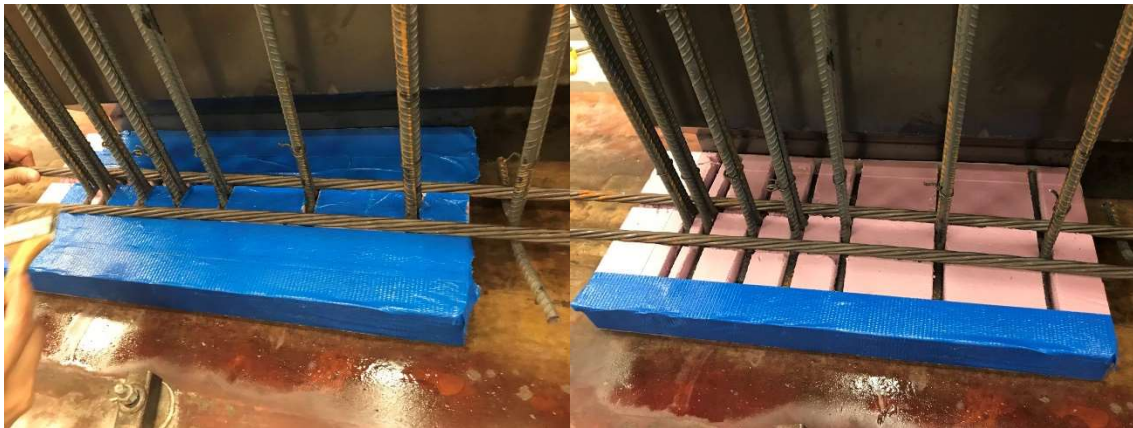
Figure 3.3: Foam Creating the Simulated Corroded Region

After that, the prestressing strands were run between the abutments and set up right above the tail of C-shape stirrups. Strands were carefully handled to avoid contact with the oil on the prestressing bed as this could affect the strand bond. Figure 3.4 shows the prestressing bed, the

19

live-end and dead-end abutments with the placement of reinforcement cage and prestressing strands. The live-end abutment attaches with hydraulic rams and pump to pull the strands with the purpose of creating tension while the dead-end abutment anchors the strands.

Figure 3.4: Dead-end Abutment (Left) and Live-end Abutment (Right) for Prestressing Bed

The prestressing strands were cut approximately 34 ft long to provide extra length beyond the prestressing bed for installing the chucks following proper procedures for pre-tensioning. Chucks were attached to all strands at the outer face of the abutments for anchoring the prestressing strands during tensioning. A 50-kip capacity load cell was placed between the chuck and the live-end abutment on one strand to monitor the instantaneous increment of applied load from the hydraulic rams. A mark was noted on the strands on the back side of the chucks from the abutments to observe and measure strand slip from the end of the chucks before, during, and after tensioning. Figure 3.5 shows the position of the mark, load cell, and chucks in preparation for pre-tensioning application.

Figure 3.5: Position of Mark, Load Cell, and Chuck in Preparation for Pre-tensioning

A ruler attached to the abutment was used to measure the elongation of the strands during tensioning (accounting for chuck slip and strand sag) to verify the load cell readings and prevent overstressing the strands. Prestressing strands were tensioned up to 75% of their ultimate strength ($f_{pu} = 270$ ksi), which is 202.5 ksi plus maximum of 1.5% of the ultimate strength, which would reach to 206.6 ksi, to account for seating of the nuts used to hold the tensioning plate. The elongation of prestressing strand was expected in range from 3.375 in. to 3.938 in. The load was applied steadily to the large steel plate at the live-end abutment to tension the strand to the target stress of 202.5 ksi (33.8 kips in tension per strand) and over the target to reach the stress of 206.6 ksi (34.5 kips in tension per strand). Next, the plate was locked at the position where the target

21

stress was reached, using four large nuts. After pre-tensioning, the prestressing bed and reinforcement cage were inspected and adjusted to ensure they had not moved or deflected during tensioning. Figure 3.6 shows the prestressing bed after pre-tensioning was completed. After all adjustments were made, the other side of the steel form was put in place, and both ends of the steel form were capsulated using piece of plywood with holes for the extended length of strands before casting concrete.

Figure 3.6: Prepared Formwork for Casting

A large rotary mixer at Fears Lab was used to mix all girder concrete and a transfer bucket was used to transport the concrete from the mixer to the girder form. The SCC mix used for girders was designed and prepared as listed in Table 3.1. A 16.75 ft^3 batch of SCC was cast for each girder. The procedure for mixing the components is as follows:

1. Wet the mixer and check to ensure there is no leak around the plug at the bottom of the mixer.

2. Add half of the High Range Water Reducer (HRWR) to the prepared mixing water used for the batch.

3. Add all the aggregate, sand, and half of the water to the mixer and mix them for 2 minutes.

4. Add all the cement and distribute the remaining water evenly to the mixer.

5. Add the remaining HRWR.

6. Blend all materials in 2-5 minutes.

7. Add more HRWR to achieve the desired workability, if necessary.

During casting each girder, the slump flow test was conducted to verify adequate workability of the SCC for compaction requirement. Also, the concrete was placed in the girder's formwork without vibration as shown in Figure 3.7. After casting, the girder was covered with plastic placed on top of the girder to ensure proper curing. Nine 4 in. x 8 in. concrete cylinder specimens were prepared when casting every girder in order to examine the compressive strength at 1 and 28 days after casting and on the girder test day. The first three cylinders were tested 24 hours after casting to determine if the concrete had reached the minimum required release strength, f'_{ci}, of 4000 psi. The next three specimens were tested at 28 days for compressive strength, f'_c.

Figure 3.7: Casting Girder without Vibration

After 24 hours, when the compressive strength test was conducted and if f'_{ci} reached at least 4000 psi, pressure was applied to the tensioning plate using the hydraulics, the nuts at the large steel plate were loosened, and the prestress force was transferred to the beam by releasing the pressure in the hydraulics. The applied load value was noted using the load cell monitor immediately before releasing the prestressing strands in order to define the jacking force (f_j) in later analysis calculations. The beams were then moved off of the prestressing bed and allowed to cure in the Fears Lab high bay. The work cycle described in this section was repeated for all nine girders.

After all girders were constructed, they were moved to specific places using a crane in Fears Lab to allow adequate space to prepare for deck placement. The composite deck formwork using design from previous research, as shown in Figure 3.8 and 3.9, was built after the girder concrete had cured for at least 28 days. The top of each girder was wetted with water and the decks were cast using ODOT Class AA concrete obtained from Dolese Bros. providing different compressive strength compared to the girders. The concrete was cast for every group of three girders along with nine 4 in. x 8 in. cylinder molds to obtain the compressive strength on the girder test day. A vibrator was used to vibrate along the girder to remove excessive air and fortify the deck concrete after placement. Wet burlap and plastic sheeting were used to cover the top of the deck and regularly watered for 7 days after casting for proper curing. In addition, the foam, which represented the corroded region, was removed from the girder after 28 days.

Figure 3.8: Deck Formwork Preparation

Figure 3.9: Casting Deck (Left) and Finishing Deck Casting (Right)

3.2.3 Repair Procedure

After the deck was cast and the foam at the bottom of the girder was removed, the surfaces around the corroded region were roughed using a grinding disk on an angle grinder for MALP and sandblasted for FR-SCC and UHPC to improve the area of contact between the conventional concrete and repair material, as shown in Figures 3.10 and 3.11. An air compressor was then operated to remove all dust on the damaged surfaces after grinding. Formwork having a dimension of 22 in. x 13 in. x 14 in for FR-SCC and MALP girders while 22 in. x 12 in. x 14 in. formwork was used for UHPC girders. These formworks would encapsulate the damaged region of the scaled AASHTO Type II girder dimensions (with some modifications) and cover the prepared surfaces. Silicone was used to seal all connections between the formwork and the girder to prevent leaking repair materials during casting, as shown in Figure 3.12.

Figure 3.10: The Representative Corroded Region without the Foam

Figure 3.11: Surface Preparation at the Corroded Region

Figure 3.12: Formwork Encapsulating the Repaired Region

When the girder surface was prepared and the formwork was set up completely, the formwork's inner surfaces were oiled before casting to prevent concrete sticking to the formwork when dismantling it and the concrete surface was wetted with a spray bottle. The oil and water were only used for casting the UHPC and FR-SCC repairs. For the MALP concrete, all surfaces and formwork must be in a dry condition. Finally, the new repair materials could be cast into the formwork following mix designs and instructions in Section 3.4.1, 3.4.2, and 3.4.3. The formwork was removed after 7 days, and the girder was tested at least 28 days after casting the repair material.

3.2.4 Repair Girder Test

The purpose of this research was to repair the corroded region of the girders, so each girder was loaded to failure to induce shear damage and examine the rehabilitated capacity of the girder after repair. After the repair materials had been allowed to cure for 28 days, each girder was transferred to the experimental zone to prepare for testing. Figure 3.13 shows a single point load was applied to the girder on a simply supported span using a load frame and hydraulic cylinder. A load cell was installed at the same position of the hydraulic cylinder to monitor the applied loads on the girder. The girder was supported on concrete blocks and elastomeric pads at both ends. During the experimental process, these pads were compressed a small amount, which was measured as deflection, but this value was neglected in subsequent calculations.
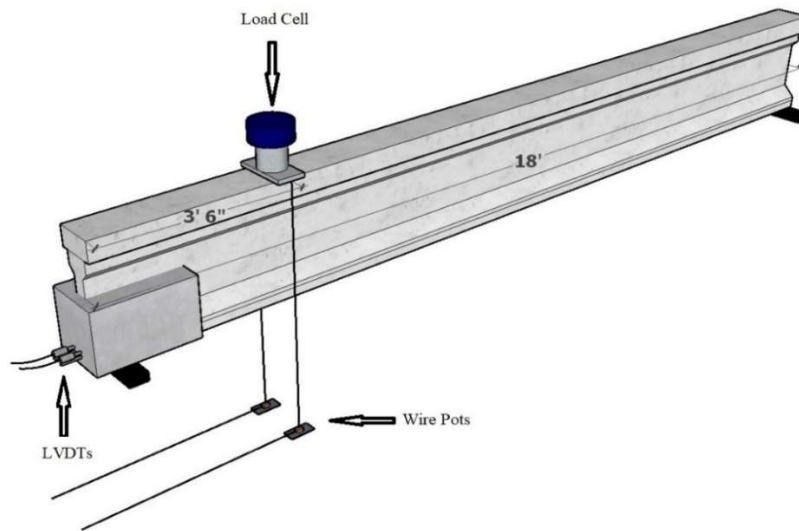
(a)

(b)

Figure 3.13: (a) Test Set Up Drawn using Sketchup and (b) Actual Test Set Up

Before each test, four linear variable differential transformers (LVDTs) were mounted to the extended length of prestressing strands to measure the strand slip. The deflection of the girder was measured directly under the point load using two-wire potentiometers (pots), one on each side of the beam. Then, all sensors were connected to a single data acquisition system to gather all data during testing.

Load was applied in 5 kips increments and the girder was examined for cracks after each increment until the appearance of shear cracks. After the first crack was observed on the girder, the loading increment was decreased to 2 kips to improve the precision of tracking crack propagation. Cracks that occurred at every load increment were marked on the surface of the

girder and the repair material, which was used to help to identify the crack relative to the applied loads and the failure mechanism of the girder. Each girder was loaded until it could no longer sustain load or when additional loading was considered a safety hazard.

3.3 Bond Test

3.3.1 Introduction

Two different bond tests were performed on all three repair materials: a slant shear test and a modified splitting tensile strength test to evaluate performance of the materials and to evaluate potential for the tests for use in quality control or assurance. The modified splitting tensile strength test was conducted following the methods of ASTM C496 Standard Test Method for Splitting Tensile Strength of Cylindrical Concrete Specimens. The loading arrangement in this test creates a tension stress perpendicular to the cylinder diameter, which can be related to bond strength between the two materials. The slant shear test was based on the methods of ASTM C882 Standard Test Method for Bond Strength of Epoxy-Resin Systems Used with Concrete by Slant Shear. The slant shear test was also utilized to evaluate the strength of a bond system formed by two regions of different concrete with an inclined interface.

3.3.2 Preparation

3.3.2.1 Modified Splitting Tensile Specimens

According to ASTM C496, 4 in. x 8 in. cylindrical molds were used for casting the base concrete and repair materials. The preparation process began with cutting a thin layer of wood with dimensions of 4 in. x 8 in. The thin wood layer was placed at the middle of the cylindrical

mold to separate two regions in which the conventional concrete was cast on one region while the other region remained empty. Next, oil was sprayed into the mold to prevent concrete sticking to the mold surface and the wood layer. The conventional concrete using for this experiment was the same as the concrete used for casting girders as specified in Section 3.2. At 14 days after casting the conventional concrete, the wood layer was taken out of the mold, and the half specimen was sandblasted to roughen the surface in order to create more area of contact and a consistent surface for casting the repair materials. After 28 days, the half specimen was returned to the mold and prewetted and the repair material was cast into the empty region directly against the conventional concrete. However, the concrete surface of the conventional concrete half specimens for MALP must be dry before casting. The repair materials were designed and cast as specified in Section 3.4.1, 3.4.2, and 3.4.3. Then, the molds containing the composite specimens were covered with plastic for at least 7 days before submerging them in lime water until testing day, except for MALP specimens.

3.3.2.2 Slant Shear Specimens

The 6 in. x 12 in. cylindrical molds were used for a slant shear test based on ASTM C882 Standard Test Method for Bond Strength of Epoxy-Resin Systems Used with Concrete by Slant Shear and examined in previous UHPC research at OU (Coleman, 2018 and Funderburg, 2018). The cylinder molds were first oiled before being placed on a crafted incline table for casting the conventional concrete half specimen portion, using the concrete specified in Section 3.2. At 7 days after placement of the conventional concrete, the half specimens were extracted from the molds and sandblasted to increase the area of contact of the conventional concrete and create a consistent surface, which was prewetted by spraying water for the UHPC and FR-SCC

specimens. However, these specimens prepared for casting with MALP could not be prewetted as instructed. Then, the UHPC, FR-SCC, and MALP concrete materials were filled in the remaining volume of these cylinders following instruction in Section 3.4.1, 3.4.2, and 3.4.3. The curing process would continue for 28 days after casting the new concrete materials. For the curing process, FR-SCC and UHPC specimens were demolded after 7-10 days and submerged in lime water to ensure hydration of concrete. The MALP specimens were kept in air dry condition covered using plastics for curing.

3.3.3 Testing

3.3.3.1 Modified Splitting Tensile Strength Test

      After 28 days, all specimens were ready to test. The tests were conducted using the Forney compression machine and set up as shown in Figure 3.14 and 3.15 based on ASTM C496. Based on Figure 3.15, the vertical load from compression machine would create the lateral tensile stress in cylinder and split it in tension along the cylinder's diameter or at the interface between the two concrete materials.

Figure 3.14: Splitting Tensile Strength Test Set Up
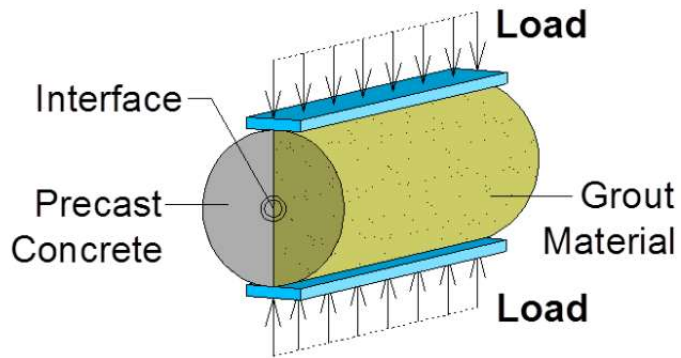
Figure 3.15: Load Application Splitting Tensile Strength Bond Test (Graybeal, 2016)

Figure 3.16: Specimen Break at Maximum Stress (Left) and Specimen Separated in Half After Test (Right)

Before testing, the dimensions of specimens were recorded to calculate the stress after the test. During and after testing, the load data was monitored and recorded. Then, the stress applied on the specimen was computed based on Equation 1.

$$T = \frac{2P}{\pi l d} \qquad (1)$$

where:

T = splitting tensile strength, psi,

P = maximum applied load indicated by the testing machine, lbf,

l = specimen length, in., and

d = specimen diameter, in.

3.3.3.2 Slant Shear Test

After 28 days, the composite cylinders were end ground to make both top and bottom surfaces flat in order to avoid the uneven stress distribution during the testing process. Finally, all specimens were placed under the Forney compression machine and tested to failure based on the instructions from ASTM C882, as shown in Figures 3.16 and 3.17. As illustrated in Figure 3.18, the vertical load would produce a stress on the interface between two concrete materials by a shear force that applies across the interface between two concrete materials.

Figure 3.17: Slant Shear Test Set Up
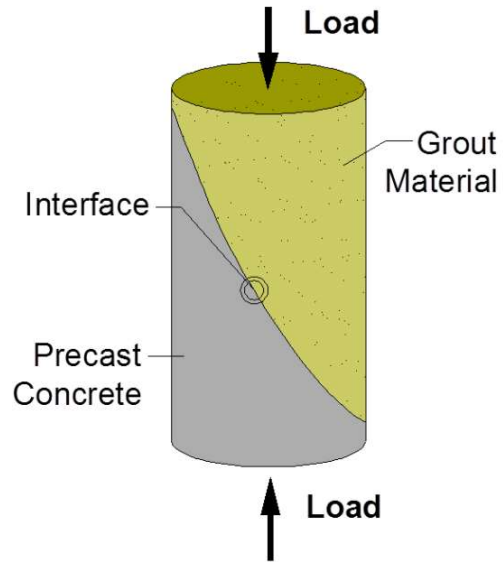
Figure 3.18: Illustration of load application in Slant Shear Bond Test (Graybeal, 2016)

Figure 3.19: Specimen Break at Maximum Stress (Left) and Specimen Separated at the Inclined Surface (Right)

Before casting the repair material, dimensions of the half specimens were noted. After testing, the load data was recorded to calculate the stress applied on the interface between the conventional concrete and repair materials. Equation 2 was used to compute the inclined stress.

$$S = 0.7854ab \qquad (2)$$

where:

S = bond strength on inclined surface of a specimen

a, b = the length of the two axes for the areas of an ellipse

3.4 Repair Material Mix Design and Preparation

3.4.1 UHPC Mix

The non-proprietary UHPC mix design, named J3, used for this research was developed at the Fears Lab of the University of Oklahoma (McDaniel, 2017). The mix proportion is listed in Table 3.2. The mix procedure was conducted as follows:

1. Half of the HRWR was added to the mixing water.

2. The oven-dry sand was added to the mixer.

3. All cementitious materials such as cement, slag, and silica fume were poured into the mixer and blended with sand for 10 minutes in a dry condition.

4. Water containing the HRWR was put in the mix gradually over 2 minutes. At this time, all components were mixed for one minute before adding the rest of the HRWR over the course of one minute.

5. The batch was blended for 8-10 minutes or until the mixture changed its form from a dry condition to a mixed fluid. Once the mix was in a fluid state, prepared steel fibers were

added evenly to the batch and the mixer kept blending in order to distribute the steel fiber

uniformly in the concrete.

6. When the 0.72-cubic-foot batch was ready to cast, the flow test (ASTM C1856) was

   conducted to verify its appropriate flowability of 8-10 inches for casting.

The UHPC mix was transported from the mixer to the repair forms using 5-gallon buckets.

Also, eight oiled cylinder molds with dimension of 3 in. x 6 in. were cast for compressive tests at

1 day, 28 days, and test day. As shown in Figure 3.18, the damaged sections of the girders were

completely repaired with UHPC.

Table 3.2: UHPC Mix Design Quantities

Material	Quantity
Type I Cement (lb/yd^3)	1179.6
Slag (lb/yd^3)	589.8
Silica Fume (lb/yd^3)	196.6
w/cm	0.2
Water (lb/yd^3)	393.2
Fine Masory Sand (lb/yd^3)	1966.0
Steel Fiber (%)	2.0
Steel Fiber (lb/yd^3)	264.5
Glenium 7920 (oz/cwt)	18.0
Glenium 7920 (lb/yd^3)	22.1

In Table 3.2, w/cm is defined as the ratio of the weight of water to the total weight of cementitious materials.

Figure 3.20: Finished UHPC Repaired Region at Front View (Left) and Side View (Right)

3.4.2 FR-SCC Mix

The FR-SCC mix design used in this research was developed by Wirkman (2016) and Choate (2018), and several trial batches were carried out before the batches used for test specimens were blended because of the sensitivity of FR-SCC to changing ambient conditions. Table 3.3 shows the mix proportion materials in weight of pounds per cubic yard before adjusting to the actual batch size required for the test specimens. The aggregates in Table 3.3 are considered in the saturated surface dry condition and needed to be adjusted to for the actual moisture content of the sand and coarse aggregate at the time of testing, and the HRWR had to be adjusted for the ambient temperature.

Table 3.3: FR-SCC Mix Design Quantities

Material	Quantity
Type I Cement (lb/yd^3)	412.5
Type K Cement (Komponent) (lb/yd^3)	112.6
Fly Ash (lb/yd^3)	224.9
Water (lb/yd^3)	229.8
Fine Aggregate (lb/yd^3)	1441.0
Coarse Aggregate (lb/yd^3)	1275.7
Air Entrainer (Master Builders AE-90) (lb/yd^3)	0.54
Glenium 7920 (HRWR) (lb/yd^3)	4.02
Polypropylene Fiber (lb/yd^3)	7.7
Citric Acid (lb/yd^3)	0.4

The mixing process for FR-SCC was conducted following these steps:

1. Add the air entrainer into the fine aggregate.

2. Add all aggregates with half the amount of water into the mixer and blend the mix for one minute.

3. Add fly ash, Type I cement, and Komponent immediately.

4. Add HRWR and the remaining amount of water slowly until reaching the desired flow.

5. Add the polypropylene fibers along with a full dose of citric acid.

6. Mix all components for 3 minutes, then let them rest for 3 minutes, and then resume mixing for 2 minutes.

7. Add a full dose of citric acid every 15 minutes to retard the set of cement while keeping the mixer rotating during casting process. The citric acid dose is reduced proportionally to the amount of remaining concrete in the mixer.

As with FR-SCC, the repaired zone was wetted with water to avoid the absorption of water from the FR-SCC into the girder's surface. During the casting process, the slump flow test (ASTM C1611) was performed to verify the flowability of the FR-SCC batch. The mix was transported using the concrete transfer bucket and poured into the formwork from one side of the girder in order to avoid entrapping air below the bottom flange. The mix transfer process was the same as for UHPC. When the FR-SCC hardened, the formwork was removed, as shown in Figure 3.19. In contrast to UHPC, eight 6 in. x 12 in. cylinders were cast for determining the compressive strength. The size of the 2.1 in. long polypropylene fibers required the size of mold to be increased.

Figure 3.21: Finished FR-SCC Repaired Girder

3.4.3 MALP Concrete Mix

The MALP material used in this research was a two-part mixture marketed under the name Phoscrete. According to the manufacture's instruction, a bag of magnesium-alumino-aggregate dry powder is mixed with a jug of the liquid phosphate activator without water or other liquids. Both the dry powder and liquid activator bottle were kept in the cool environmentally controlled room (approximately 72 °F) to slow down the chemical reaction during mixing and the setting time of the concrete. First, the liquid activator was poured into a dry plastic bucket before adding the dry aggregate powder. A urethane auger paddle provided by Phoscrete was then used to mix these two components for one minute. The mixture was placed in the formwork immediately after mixing not only to avoid the concrete hardening quickly before it flowed into the formwork, but also to begin the next batch as soon as the first was completed. For the damaged region, MALP was cast from one side first to ensure the concrete flow along the formwork and prevent entrapping air. Until the concrete was filled up to the half-height of the formwork, the MALP was poured alternatively from both sides of the formwork to balance the height of the repair material. A steel rod was used to compact the MALP in order to avoid honeycombing and fill any remaining voids. A total of nine 4 in. x 8 in. cylindrical molds were used to cast MALP at the same time with casting a girder. These specimens were tested to determine the compressive strength at 1 day, 28 days, and test day. Figure 3.20 shows the completed repaired girder with MALP.

Figure 3.22: Finished MALP Repaired Girder

Chapter 4 Results

4.1 Bond Test Result

Table 4.1 shows the experimental values from the slant shear tests and the splitting tensile strength composite specimens of the three repair materials and conventional concrete. These values represent the bond stress on the calculated interface area for the slant shear tests and the tensile stress on the interface for the splitting tensile strength specimens. For each repair material, three slant shear specimens were cast and tested, then the average value from the three tests was calculated for each material. The results indicated significant differences between each repair material, especially between UHPC and MALP. The UHPC material exhibited the highest bond strength while the MALP material had the lowest values. Figure 4.1 shows the tested slant shear specimens after breaking at the inclined interface area between repair materials and the conventional concrete following AASHTO C882. Based on Figure 4.1, the bond failure mechanism could be predicted under compression for the repair material in the actual girder experiments. As for the splitting tensile test following AASHTO C496, three cylindrical specimens were tested for each repair material, in which specimens failed at the vertical interface between the two materials. Figure 4.2 illustrates the surfaces of the half-cylinder specimens after breaking which reflected the bond failure mechanism under tension.

Table 4.1: Splitting Tensile Test and Slant Shear Test Results

Required Material	Splitting Tensile Stress, psi	Slant Shear Stress, psi
MALP	235	550
FR-SCC	455	2300
UHPC	610	4420

Figure 4.1: Specimen after Slant Shear Test

Figure 4.2: Specimen after Splitting Tensile Test at Side View (Left) and Top View (Right)

As described above, although both bond tests utilize different methods, they have the

same purpose of determining strength of bond between new repair materials and conventional

concrete. The UHPC and even FR-SCC splitting tensile stress results are in range of the conventional concrete's tensile stress when testing a cylindrical specimen with no bond interface. Therefore, as there is no reinforcement in the cylindrical specimen, the tensile stress of the composite cylindrical specimens of UHPC and FR-SCC with conventional concrete behaves like uniform conventional concrete specimens. For slant shear test results, they were larger values compared to tensile stress results due to the compression force on the large inclined interface area.

For the splitting tensile strength consistency, the difference between the highest and the lowest values was a maximum of approximately 13.5% for each set of three specimens. However, the slant shear test results were consistent for only UHPC and FR-SCC materials as the differences between the highest and the lowest values were approximately 16% and 19% for UHPC and FR-SCC, respectively. MALP had significant difference between the highest and the lowest values, 38%, so the MALP tests were less consistent. Another goal of using one of these tests is for control/quality assurance measurement. As will be seen in Section 4.4, the results from both bond tests and the girder tests had similar trends, which could fortify the goal of using one of those tests for control/quality assurance measurements.

4.2 Compressive Strength of Concrete

Most of the girders had a compressive strength exceeding the targets of 4000 psi for 1-day strength, and 7000 psi for 28-day strength, presented in Table 4.2. However, the first girder (MALP-1) had lower value than target for both 1-day and 28-day strengths, which was not consistent with other girders. Additionally, the compressive strengths for girders MALP-1 and

MALP-2 on test day were lower than the 28-day compressive strengths. On the other hand, there was no abnormal behavior observed while testing the MALP-1 and MALP-2 girders, which substantiated sufficient compressive strength for adequate girder performance. The issue for these specimens could be related to compressive test specimen preparation and ambient temperature on casting day. An uneven surface on one or both of the top and bottom surfaces of the specimens after grinding could lead to unbalanced distribution of stress on the specimens. Another possibility is that there may have been problems with the cylinders' consolidation while setting up and casting. The ambient temperature was recorded as 95°F on casting day for MALP-1 while it was 89°F on casting day for MALP-2. The compressive strengths of the deck were noted as 6840 psi, 6920 psi, and 7030 psi at 28 days. In fact, the deck, and compressive strengths of the two sets of MALP-1 and MALP-2 specimens may have been switched because of a labeling error; therefore, it was not clear which specimens were tested for the MALP-1, and MALP-2 two girders and the associated deck. Therefore, the 28-day compressive strength of 7000 psi (7 ksi) was conservatively used as the base value for analysis.

In addition, because of missing data for compressive strengths of the UHPC girders at 28 days, the average data from the closest casting beams (MALP-3, FR-SCC-3, and UHPC-1) was used to represent the compressive strength at 28 days for the UHPC girders.

It should be noted that there may be some size effect related to the concrete cylinders used for compressive strength of the repair materials when comparing those values. The UHPC compressive strength was measured with 3 x 6 in. cylinders, MALP used 4 x 8 in. cylinders, and FR-SCC used 6 x 12 in. cylinders. Day (1994) found that in the range of 2,900 psi to 14,500 psi, compressive strength of 4 x 8 in. concrete cylinders was expected to be higher than for 6 x12 in. concrete cylinders by approximately 5%. However, in range between 2,900 psi and 8,700 psi, the

compressive strength of both types of concrete cylinder could be assumed equal. Day (1994) also stated that "the coefficient of variation for 4 x 8 in. cylinders is equivalent to that of 6 x 12 in. cylinders over a broad range that encompasses normal, high, and very high-strength concrete." The current ASTM standard for testing UHPC compressive strength, ASTM C1856, specifies that 3 x 6 in. cylinders should be used. Therefore, the size effect was not taken to be a major concern for comparing compressive strength in this research.

Table 4.2: Compressive Strength of Conventional Concrete Girder Specimens

Repair Material and Test Number		MALP-1	MALP-2	MALP-3	FR-SCC-1	FR-SCC-2	FR-SCC-3	UHPC-1	UHPC-2	UHPC-3
Compressive Strength, psi	1-day	3910	5950	4540	6270	5190	5900	5220	5940	6020
	28-day	6580	8010	7060	6680	7720	7980	7850	8270	8620
	Test-day	5910	7660	7800	6490	8530	7660		8000	
	Repair Material	7070	7100	7120	9640	8460	8460	15770	16090	14810

4.3 Repaired Girders

In order to examine the result of the experimental tests, data from two undamaged reference beams with the same design and constructed with the same concrete was used for comparison in several graphs of deflection and slip for each tested girder. The undamaged reference beams noted as M1-U and M4-U, were built and tested as part of a related research project conducted by Ahmadi (2021). These two specimens were selected as representative of the upper and lower bound behavior of all undamaged specimens tested by (Ahmadi, 2021).

4.3.1 MALP Girders

4.3.1.1 MALP-1 Girder

    4.3.1.1.1 Overview

    The shear force was induced on the repaired beam end by applying a point load at 3.5 ft

from the simulated corroded end of the girder, as described in Section 3.2.4 and Figure 3.13. The

load was increased gradually, and the relative deflection and strand slip were monitored. For this

girder a layer of repair material was cast first, but the repair was stopped due to high

temperatures. Later on, additional repair layers were cast. The behavior of the girder may have

been affected for this reason. Figure 4.3 shows the appearance of cracks on the girder after

testing. There was no crack observed in the repair region, which means the repair was

successfully designed to handle the load and the failure zone was moved away from the

simulated corroded end region. During the experiment, there was no delamination or differential

movement observed between the girder and the repair. The specimen failure started with a

flexure/flexure-shear crack at web of the girder extending away from the junction of the repair

material and the girder. This crack was observed to be the widest at the point of failure and

potentially led to the failure of the girder. The cracks generated upward diagonally as they

moved to the loading point and vertically downward to the bottom flange. At 39 kips, it was

observed that there was a crack started at the junction between the girder and MALP concrete.

When the applied load was approaching 43 kips, the deck started crushing at the load point and

the loading was stopped at the same time. Therefore, the maximum capacity of the girder was

just under 43 kips.

Figure 4.3: MALP-1 Girder after Test

4.3.1.1.2 Load vs. Deflection Behavior of MALP-1 Girder

As described in Figure 3.13, a load cell and two wire-pots were used to monitor the load

and deflection during testing. Figure 4.4 shows the load-deflection response of girder MALP-1

compared to the two undamaged reference beams. The three graphs were placed in the same

figure in order to compare how the girder was rehabilitated compared to the expected undamaged

specimen behavior after applying new repair material. The first crack was a flexure-shear crack

noted at 35 kips of load from the bottom of the girder and went through the web. There was a

significant drop in load and increase in deflection at the same time when the first crack occurred,

which was indicative of a significant crack. After the first crack occurred, the stiffness of the

girder was reduced significantly and only load increased gradually while the deflection increased

considerably. The MALP-1 girder had significantly lower capacity and higher deflection at

failure when compared to the undamaged M1-U (lower bound) and M3-U (upper bound)

specimens. The peak load for MALP-1 was 43 kips and the peak deflection was 0.65 in. In

comparison, girder M1-U had a maximum capacity of 50 kips with 0.305 in. deflection while

girder M3-U had a peak load of 54 kips with 0.51 in. of deflection. In addition, the peak load measured for the MALP-1 girder was less than the estimated capacity calculated in Appendix 7.3 and 7.4.
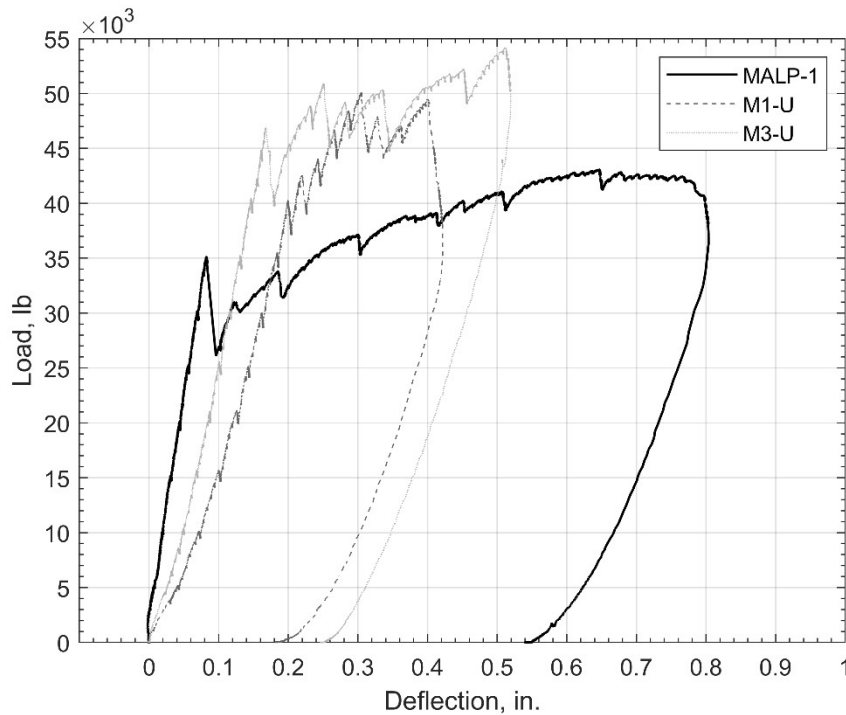
Figure 4.4: Load vs. Deflection Curves of MALP-1 Girder and Undamaged Reference Beams

As seen in Figure 4.3, MALP-1 started cracking at 35 kips, which was earlier than for the undamaged reference beams. However, the initial slope of the MALP-1 load vs. deflection curve was larger than the original beams, which indicates that the stiffness of MALP-1 was improved compared to the other beams. The MALP-1 girder's peak load was less than the undamaged reference beams, which were artificially stopped to reach a specific damage state and not reaching their limit state, but its maximum deflection was larger as shown in Figure 4.4.

4.3.1.1.3 Load vs. Slip Behavior and Failure Mechanism of MALP-1 Girder

Strand slip was calculated by averaging the measured values from both LVDTs at the end of girder close to the loading point. However, there was an extremely small amount of strand slip measured for the MALP-1 girder; therefore, the curve of load vs. slip in Figure 4.5 looked like a vertical line. Figure 4.5 shows the strand slip and the deflection of the MALP-1 girder relative to load to show the relative timing between occurrence of slip and deflection. In addition, the crack pattern showed that most of the cracks were inclined and started in the web near the girder end. Based on these factors, the failure mechanism was determined to be a bond-shear failure using criteria from previous research (Naji, Ross, & Floyd, 2016).
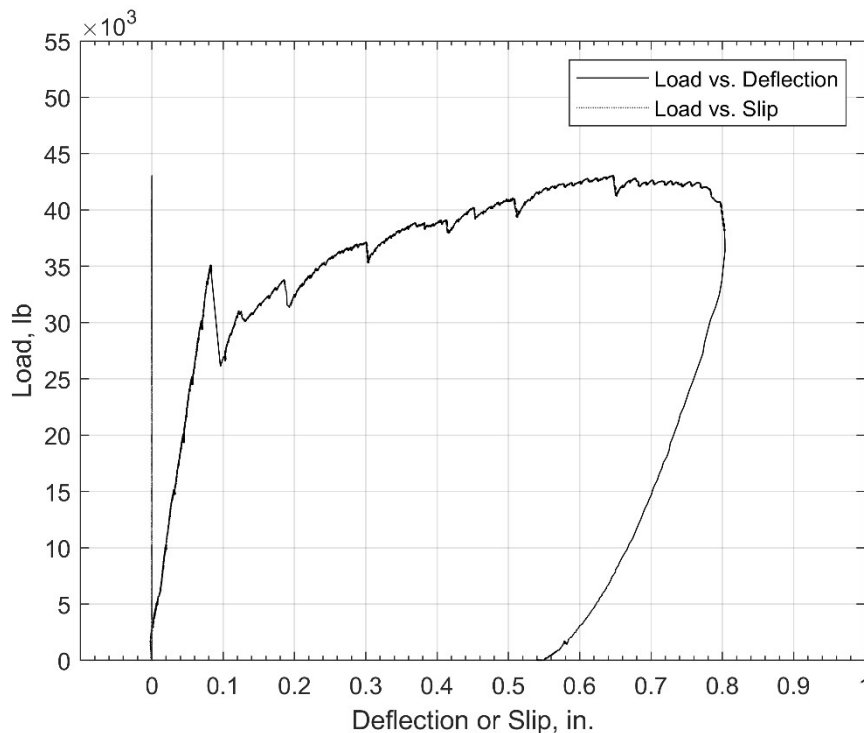
Figure 4.5: Load vs. Deflection and Load vs. Slip Curves of MALP-1 Girder

4.3.1.2 MALP-2 Girder

4.3.1.2.1 Overview

Figure 4.6 shows repair girder MALP-2 after testing. The first flexure-shear crack appeared in the web of the girder, at the junction between the repair material and the girder, and approximately an inch away from the repair material. As the load increased, the crack developed slightly vertically before it propagated upward towards the loading point and downward to the bottom flange of the girder. Other flexure and flexure-shear cracks beginning at the bottom flange of the girder were observed at the load of 37 kips and 39 kips. The maximum load of 42.6 kips was noted at the point of crushing of the girder's deck.

Figure 4.6: MALP-2 Girder after Test with SW Side (Left) and SE Side (Right)

4.3.1.2.2 Load vs. Deflection Behavior of MALP-2 Girder

The load vs. deflection curve for the MALP-2 girder is shown in Figure 4.7. There were several similar points between the MALP-1 and MALP-2 girders. The MALP-2 girder started cracking at 35 kips of load and its initial load vs. deflection curve slope was larger than for the

original, undamaged reference beams. At the point the first crack occurred, there was a sharp

drop in load, approximately 10 kips, and the stiffness of the girder was reduced. However, as

compared to girders M1-U and M3-U which were artificially stopped before reaching the

ultimate limit state, the MALP-2 girder had a deflection of 0.84 in. at the peak load (42.6 kips).

An issue occurred with the data collection equipment at a load of 25 kips, which is visible as a

horizontal line in Figure 4.7. Deflection data for girder MALP-2 was observed to move

backward then returned. This issue could come from the unstable electric current of the data

collecting system, noise of data collection or from someone bumping the instrument. In addition,

the MALP-2 girder's measured capacity was les than the calculated capacity presented in

Appendix 7.3 and 7.4.
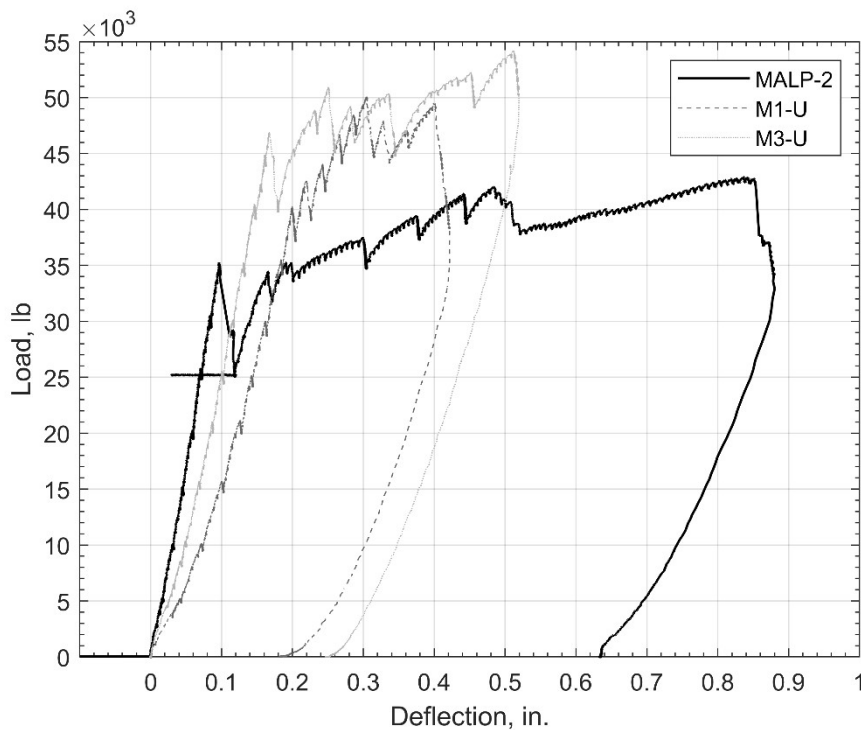
Figure 4.7: Load vs. Deflection Curves of MALP-2 Girder and Undamaged Reference Beams

4.3.1.2.3 Load vs. Slip Behavior and Failure Mechanism of MALP-2 Girder

Figure 4.8 shows the load vs. deflection and load vs. slip curves for the MALP-2 girder to identify the relationship between the two. The comparison indicates the web shear and flexure-shear cracks that started at 35 kips correspond with the initial strand slip. In addition, there was a large amount of strand slip change after the first crack that indicated the significance of the contribution of bond to the overall failure for girder MALP-2. Unlike the MALP-1 girder, the MALP-2 girder's peak load was associated with the flange crushing in compression. In addition, a crack was observed adjacent to the support which opened widely due to strand slip as load increased, as shown in Figure 4.6. Also, the peak load of the MALP-2 girder was less than the nominal flexural capacity. These items together indicate that the failure of MALP-1 was bond-flexure failure based on the criteria of Naji et al. (2016).
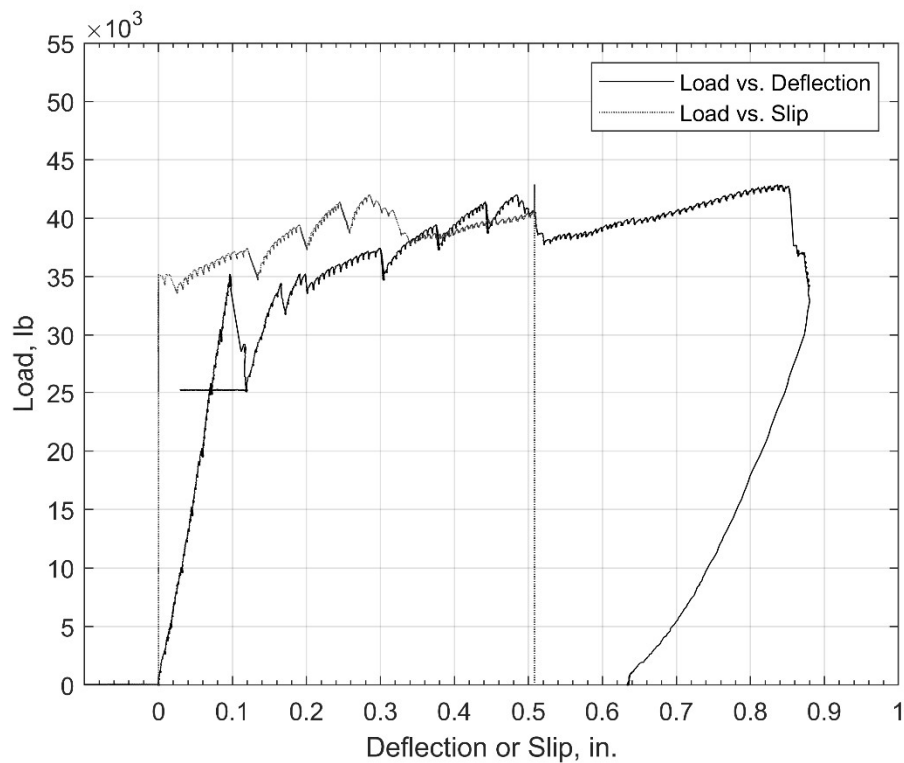
Figure 4.8: Load vs. Deflection and Load vs. Slip Curves of MALP-2 Girder

4.3.1.3 MALP-3 Girder

4.3.1.3.1 Overview

The cracking pattern for the MALP-3 girder after failure is shown in Figure 4.9. The first crack for the MALP-3 girder appeared at the bottom flange approximately 8 in. away from the junction of the repair and the girder on the SW side. Similar to both other MALP girders, the crack started nearly vertical in the bottom flange and at the web began propagating toward to the loading point. In contrast to MALP-1 and MALP-2, the first crack occurred early for MALP-3, at a load of 30 kips and at the bottom flange. In addition, when the load reached 43 kips, there was a crack observed at the junction of the girder and the repair and passing through the MALP repair material.

Figure 4.9: MALP-3 Girder after Test with SW Side (Left) and SE Side (Right)

4.3.1.3.2 Load vs. Deflection Behavior of MALP-3 Girder

Figure 4.10 shows the load vs. deflection curve of the MALP-3 girder with those of the two undamaged reference beams. Unlike MALP-1 and MALP-2, there was a significant increase in load after the first crack for MALP-3 with limited deflection, which indicated a higher stiffness of the girder after cracking compared to the MALP-1 and MALP-2 girders. The peak load of 46.4 kips was observed as the deck started crushing and with 0.69 in. deflection. In comparison to girders M1-U and M3-U, the MALP-3 girder had a lower capacity and larger deflection. Furthermore, the measured capacity of the MALP-3 girder was less than the estimated capacity computed in Appendix 7.3 and 7.4.
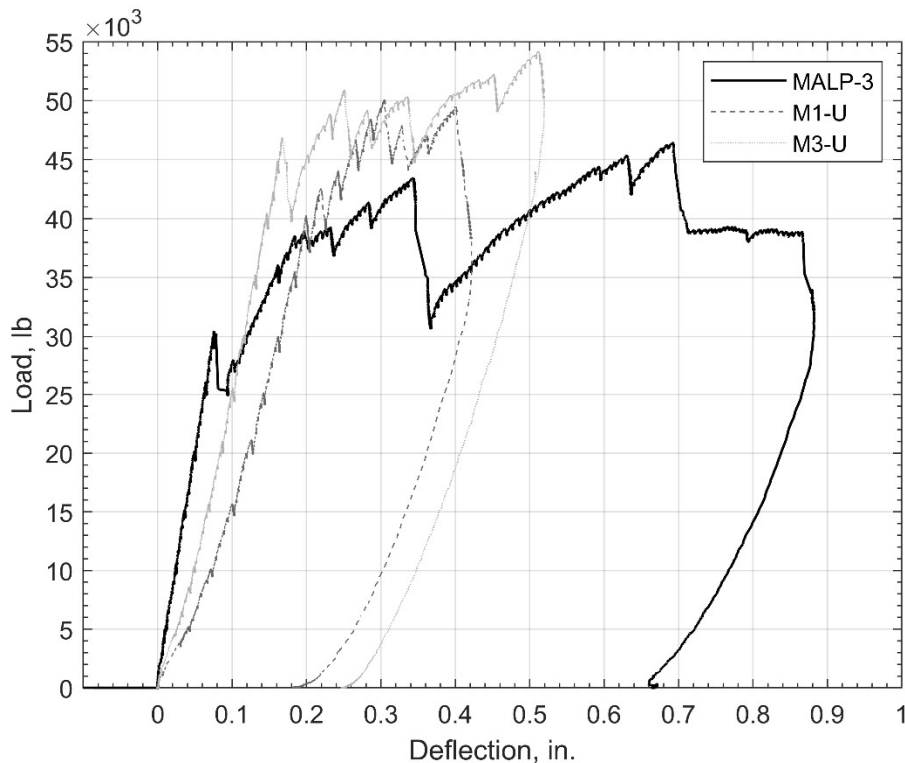
Figure 4.10: Load vs. Deflection Curves of MALP-3 Girder and Undamaged Reference Beams

4.3.1.3.3 Load vs. Slip Behavior and Failure Mechanism of MALP-3 Girder

Based on Figure 4.11, the prestressing strands began slipping at 38.5 kips of load, which was higher than the first cracking load of 30 kips. In addition, the stiffness of the girder was reduced significantly after slip was observed, which could be major difference between MALP-3 and MALP-1 and 2. It should be noted that the slip data in Figure 4.11 for the MALP-3 girder was incomplete due to the LVDT running out of measurement range. However, the significant amount of slip measured indicates a bond failure. Figure 4.9 shows that the compression zone (top flange) of the girder was crushed at 45 kips with the appearance of flexural cracks at 43 kips. The combination of the strand slip, cracking pattern, and flange crushing indicate the failure type of this girder was bond-shear/flexure.
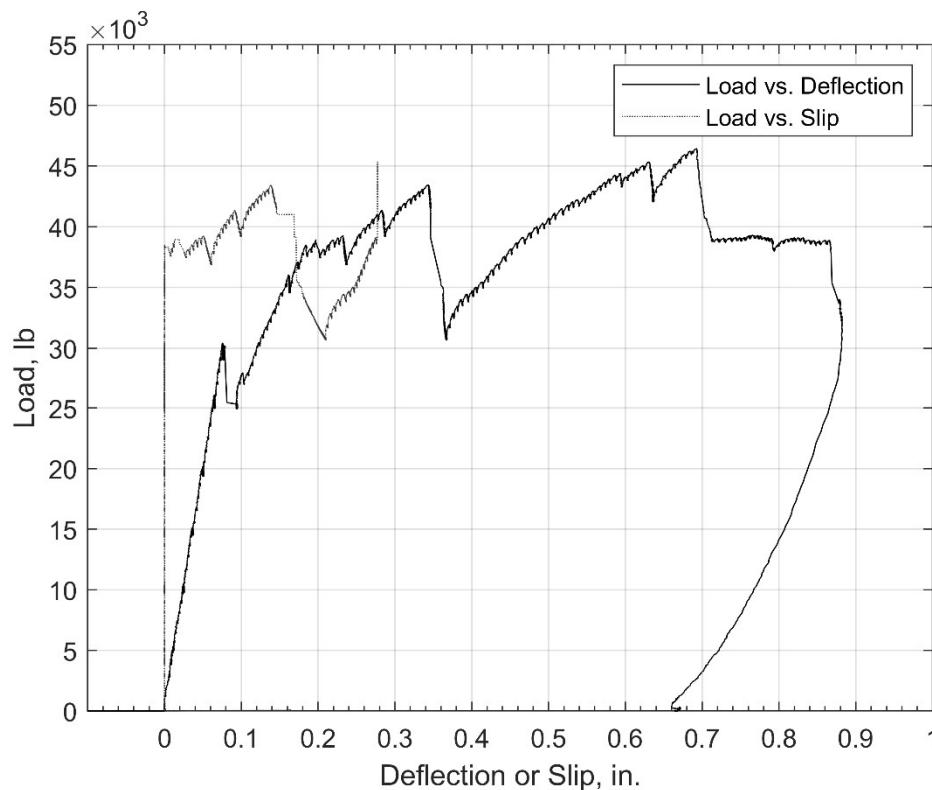
Figure 4.11: Load vs. Deflection and Load vs. Slip Curves of MALP-3 Girder

4.3.1.4 Summary of MALP Girder Tests

In summary, all MALP repair girders had a higher initial stiffness but lower capacity, higher deflection, and earlier first cracking as compared to the undamaged reference beams. However, for the simulated corroded girders the loading point was in the transfer length region (measured from the end of the damaged section) while the loading point of the undamaged reference beams was in the constant initial prestress region (with transfer length beginning at the end of the beam). It could be understood that this difference in location of the transfer length changed the bond behavior and maximum load resistance. Figure 4.12 shows that all three girders exhibited very similar behavior including some ductility.
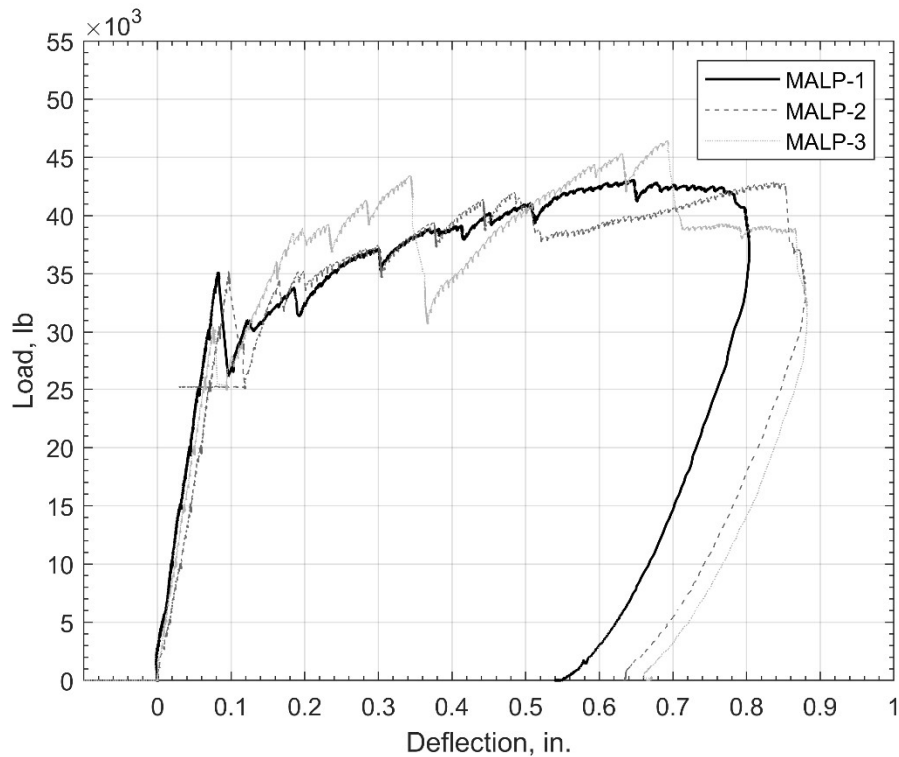
Figure 4.12: Load vs. Deflection Curves of MALP Girders

4.3.2 FR-SCC Girders

4.3.2.1 FR-SCC-1 Girder

    4.3.2.1.1 Overview

    The cracking pattern at failure of the FR-SCC-1 girder is shown in Figure 4.12. The first

crack was a web shear crack that appeared at the middle of the web on both sides, and at the

bottom flange on SE side of the girder at a load of 30 kips, visible in Figure 4.12 and 4.13. As

the load increased, the first crack developed diagonally and propagated both upward to the

loading point, and downward to the bottom flange. Additional flexural and shear cracks appeared

as the load increased. The concrete at the junction between the FR-SCC repair and the girder

spalled before beam failure and created a crack between the two materials as shown in Figure

4.12 and 4.13. The peak load was recorded as 51 kips as the deck crushed.

Figure 4.13: FR-SCC-1 Girder after Test with SE Side (Left) and SW Side (Right)

Figure 4.14: Cracks in Bottom Flange of FR-SCC-1 Girder after Test

4.3.2.1.2 Load vs. Deflection Behavior of FR-SCC-1 Girder

Based on Figure 4.14, the FR-SCC-1 girder started cracking at a load of 30 kips indicated

by observation of the drop in load, which was less than the reference undamaged M1-U (40 kips)

and M3-U (47 kips) girders. However, the peak load of FR-SCC-1 girder was 51 kips, which was

slightly larger than the M1-U (lower bound, 50 kips), and smaller than the M3-U (upper bound,

54 kips) values. Although FR-SCC-1 did not have the largest peak load or higher cracking load

compared to both M1-U and M3-U, it had larger deflection. The maximum monitored deflection

was 1.1 in. compared to 0.4 in. (M1-U) and 0.5 in. (M3-U), which were artificially stopped

before reaching their ultimate limit state. In addition, the measured capacity of the FR-SCC-1

girder was less than the estimated capacity presented in Appendix 7.3 and 7.4.

Figure 4.15: Load vs. Deflection Curves of FR-SCC-1 Girder and Undamaged Reference Beams

4.3.2.1.3 Load vs. Slip Behavior and Failure Mechanism of FR-SCC-1 Girder

As shown in Figure 4.15, the strand did not slip as the first crack occurred because the crack occurred in the web first and had not propagated into the strands to disturb the bond. At 32 kips, the crack seemed to start disturbing the anchorage of the prestressing strand, and the strand started slipping at approximately 36 kips. The stiffness of the girder was also reduced after the strands started slipping. Thereafter, as the load increased, the strand slipped further. The cracks were also opened wider, and the deflection increased with increasing load. The slip data of FR-SCC-1 girder was stopped before completion of the test because the LVDTs run out of measurement range. The widest inclined crack was observed at the junction between the new material and the girder. Combining all factors above, the failure mechanism could be classified as bond-shear/flexure (Naji et al., 2016).

63
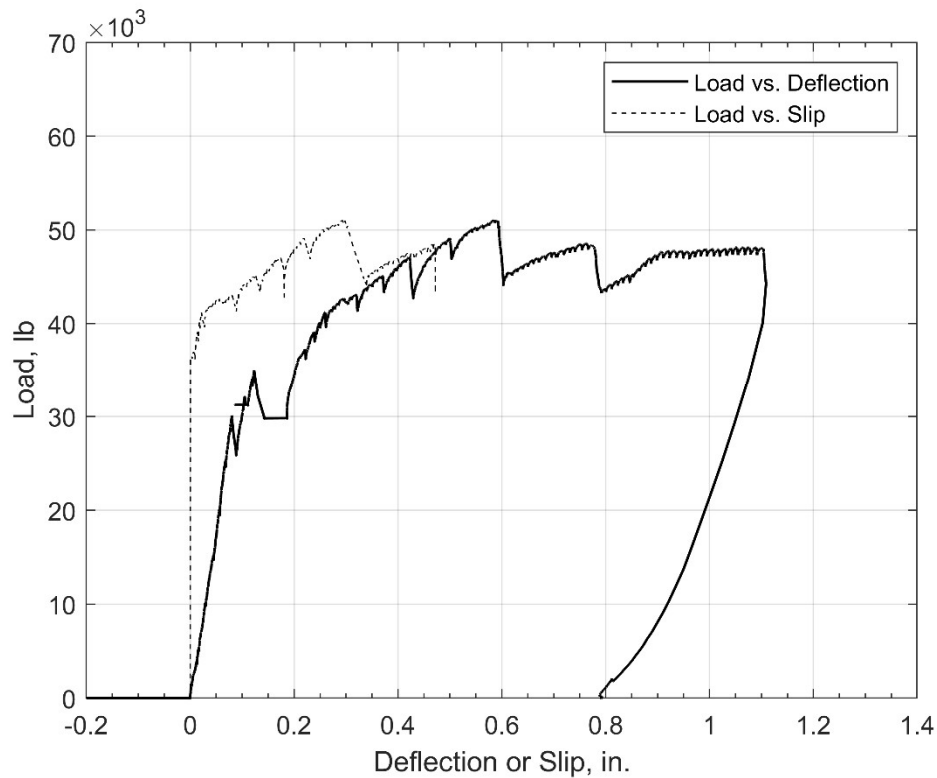
Figure 4.16: Load vs. Deflection and Load vs. Slip Curves of FR-SCC-1 Girder

4.3.2.2 FR-SCC-2 Girder

4.3.2.2.1 Overview

Figure 4.16 shows the cracking pattern at failure for girder FR-SCC-2. The first crack was a shear crack that started at an early load of 30 kips in the web of the girder. As the load increased, the crack propagated diagonally upward to the loading point, and downward to the bottom flange. There were cracks observed at the junction of the girder and FR-SCC repair, but there was no concrete spalling at the junction. Instead, the shear crack about 3 in. away from the junction of the girder and repair opened widely as the load was increased, as shown in Figure 4.16. At a load of 35 kips, there was an appearance of a flexure-shear crack extending from the

64

bottom flange into the web. Additional shear and flexural cracks occurred as the load was increased.

Figure 4.17: FR-SCC-2 Girder after Test with SE Side (Left) and SW Side (Right)

4.3.2.2.2 Load vs. Deflection Behavior of FR-SCC-2 Girder

The load-deflection curve for the FR-SCC-2 girder (Figure 4.17) shows that after initial shear crack at 30 kips, the load continued increasing until it reached the peak load of 64.6 kips and slightly dropped afterward. However, there was a significant increase after the initial crack as compared to the reference undamaged reference beam upper-bound curve (M3-U), whose initial cracking load was 47 kips and peak load was 54 kips. There was a difference of 10.6 kips or 19.6% between the maximum loads for the FR-SCC-2 girder and M3-U beam. The deflection of girder FR-SCC-2 at peak load was 0.6 in. compared to 0.51 in. (M3-U) and 0.305 in. (M1-U) for the undamaged reference beam tests. The maximum deflection of FR-SCC-2 was 1.32 in. compared to the measured values for M3-U (0.52 in.) and M1-U (0.42 in.), which were artificially stopped before reaching their ultimate limit state. The difference in deflection could be a result of the higher stiffness of the FR-SCC-2 due to the presence of the repair and better

65

bonding between the strands and repair material as compared to the two undamaged reference beams. Furthermore, the capacity of the FR-SCC-2 girder was higher than the estimated capacity computed for the non-prestressed region, but less than the value calculated for the prestressed region's capacity. Both are presented in Appendix 7.3 and 7.4
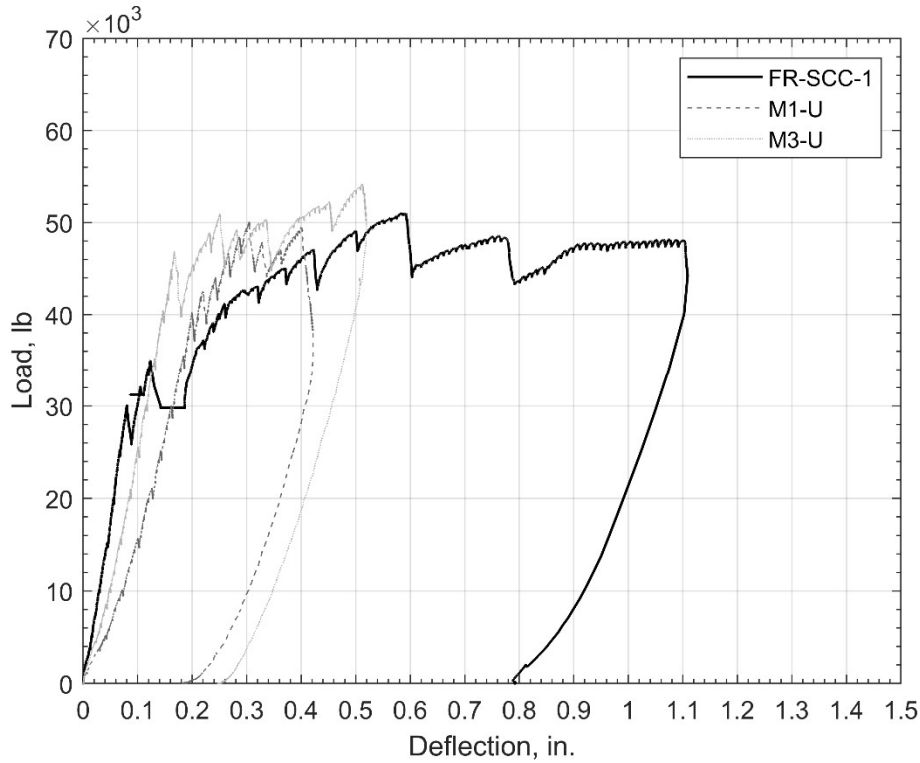

Figure 4.18: Load vs. Deflection Curves of FR-SCC-2 Girder and Undamaged Reference Beams

4.3.2.2.3 Load vs. Slip Behavior and Failure Mechanism of FR-SCC-2 Girder

Based on Figure 4.18, the initial shear and flexure-shear cracks of the girder occurred before the strands debonded. The first cracks were observed by a drop in load at 30 kips of applied load and were located in the web and near the bottom flange of the girder but had not disturbed the bond of the strands. As the load increased, the cracks propagated diagonally and opened wider which disturbed the strand bond, and the strand started slipping approximately at

66

58.2 kips, which was much higher than peak loads of M1-U and M3-U. To explain this result, the FR-SCC-2 repair concrete may have provided improved resistance to load, and better anchorage of the prestressing strands. Based on the criteria outlined by Naji et al. (2016), the failure type of the FR-SCC-2 girder was bond-shear/flexure. The slip data of FR-SCC-2 girder stopped before completion of the test because the LVDTs ran out of measurement range.
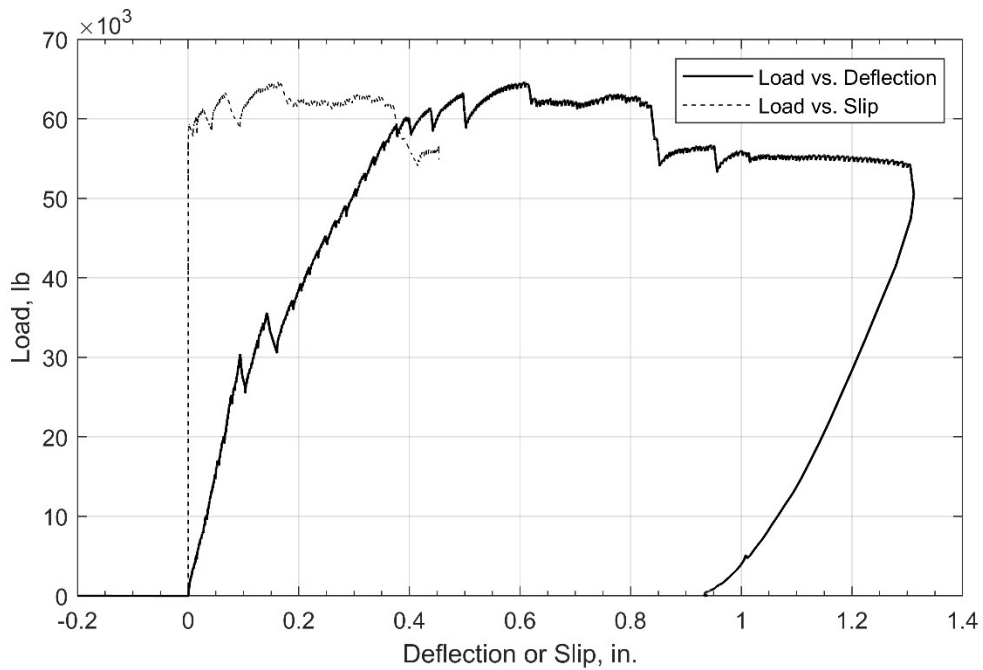
Figure 4.19: Load vs. Deflection and Load vs. Slip Curves of FR-SCC-2 Girder

4.3.2.3 FR-SCC-3 Girder

4.3.2.3.1 Overview

As shown in Figure 4.19, the initial inclined shear crack occurred at 30 kips on the web of the girder. As the applied load was increased, the initial crack propagated upward and downward diagonally. Unlike the other FR-SCC repair girders, the FR-SCC-3 girder had a crack in the new repaired region that occurred at a load of 32 kips, which was visually observed.

Additional flexural cracks occurred underneath the loading point and into the span and additional shear cracks formed in the web as load was increased. The largest crack was a flexure-shear crack observed at the bottom flange near the junction between the FR-SCC repair region and the girder on both sides. The deck was crushed after the peak load had been reached.

Figure 4.20: FR-SCC-3 Girder after Test with SE Side (Left) and SW Side (Right)

4.3.2.3.2 Load vs. Deflection Behavior of FR-SCC-3 Girder

Figure 4.20 shows the load vs. deflection curve for the FR-SCC-3 girder along with the two from undamaged reference beams. After the first crack occurred, the stiffness of the girder was reduced considerably. As load gradually increased, the deflection increased significantly. In comparison to the M1-U and M3-U beams, the FRSCC-3 girder had the first crack at 30 kips, which was much lower than for M1-U (40 kips) and M3-U (47 kips). In addition, the deflection measured for the FR-SCC-3 girder was 0.7 in. at the peak load of 56 kips. However, the measured capacity of the FR-SCC-3 girder was less than the estimated capacity calculated in Appendix 7.3 and 7.4.
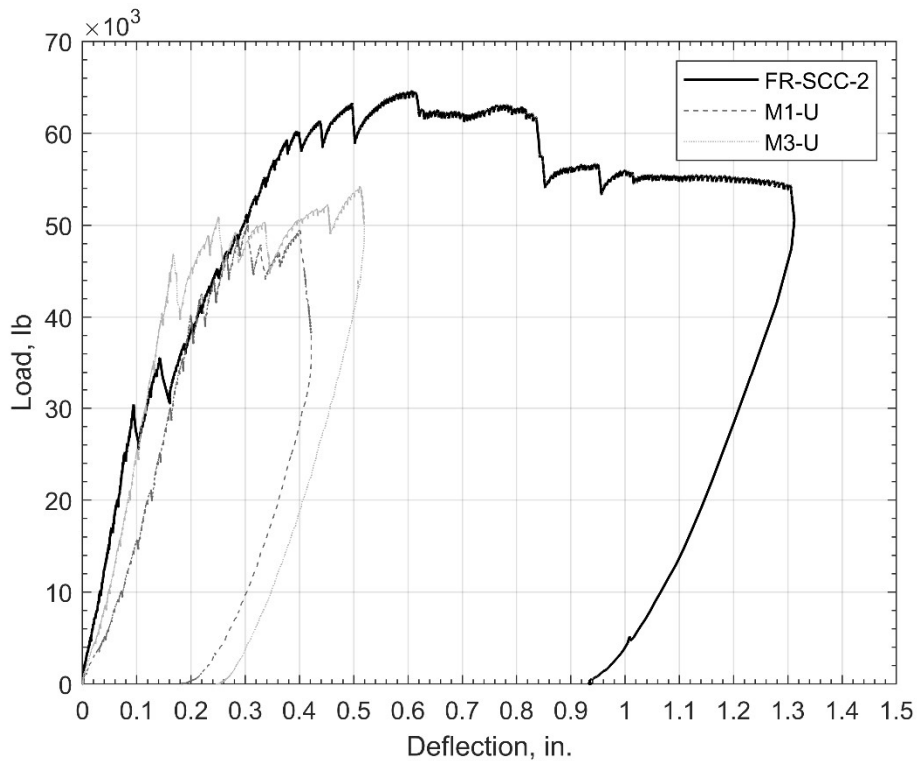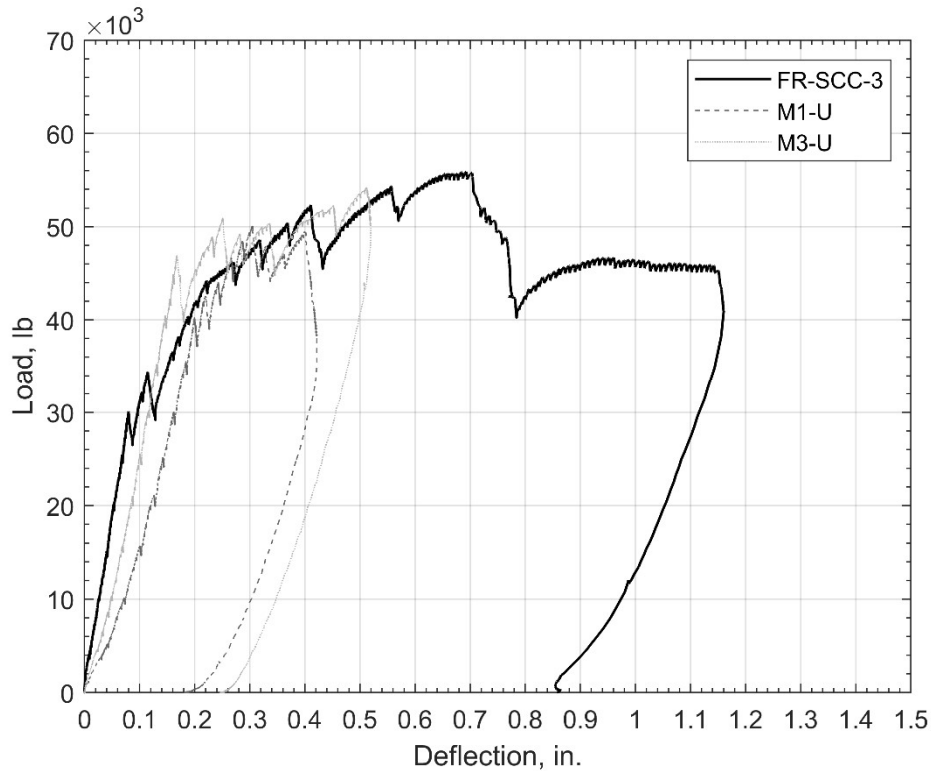
Figure 4.21: Load vs. Deflection Curves of FR-SCC-3 Girder and Undamaged Reference Beams

4.3.2.3.3 Load vs. Slip Behavior and Failure Mechanism of FR-SCC-3 Girder

The load vs. slip relationship for the FR-SCC-3 girder is shown in Figure 4.22 along with the load vs. deflection curve. In addition, the slip data of the FR-SCC-3 girder was stopped early because the LVDTs run out of measurement range. As shown in this figure, the strand started slipping at approximately 43.1 kips, which was much larger than the initial cracking load of 30 kips. The stiffness also reduced significantly after strand slip began. The major cracks were caused by shear with the appearance of a flexural crack underneath the loading point, so according to Naji et al. (2016), the failure type of this girder was classified as a bond-shear/flexure.

69
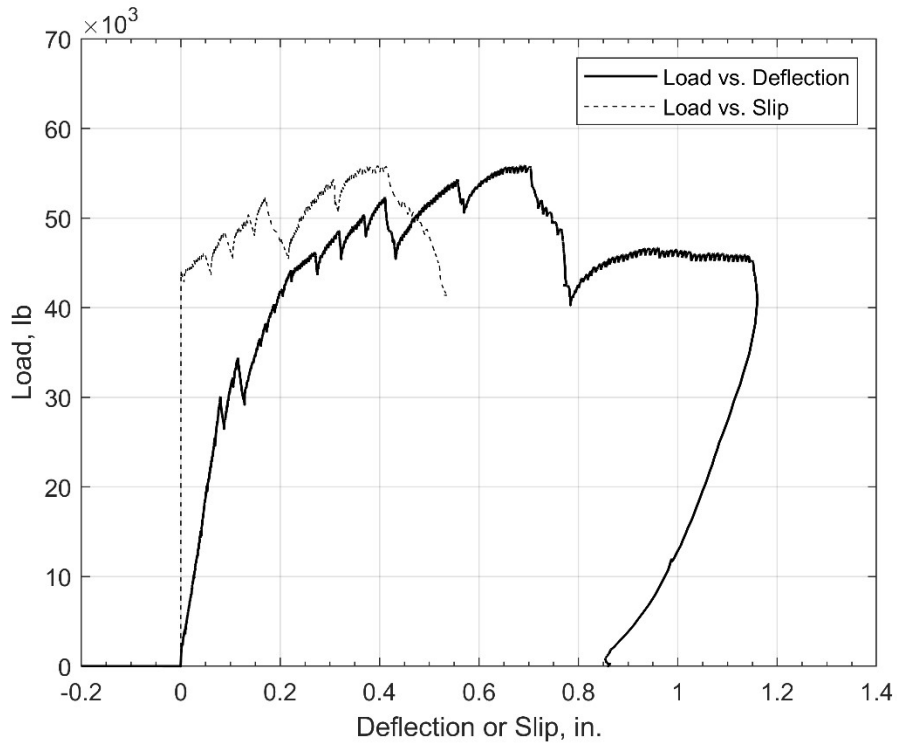
Figure 4.22: Load vs. Deflection and Load vs. Slip Curves of FR-SCC-3 Girder

4.3.2.4 Summary of FR-SCC Girder Tests

In general, the FR-SCC repair material resulted in girders that performed nearly as well, or better than the reference undamaged reference beams. The proof for this comparison was that FR-SCC repair girder load vs. deflection curves were similar to the upper bound reference girder curve (M3-U), and girder FR-SCC-2 had an even higher ultimate load. For strand slip of the FR-SCC repaired girders, the strand started slipping far further after the initial crack than for the undamaged specimens. Therefore, the FR-SCC repair material played a role as a well-performing anchorage for the prestressing strands. Figure 4.23 shows the load deflection curves for all three girders. The behavior is very similar for all three before cracking and similar patterns are visible after cracking, but with some variability in maximum load.

70
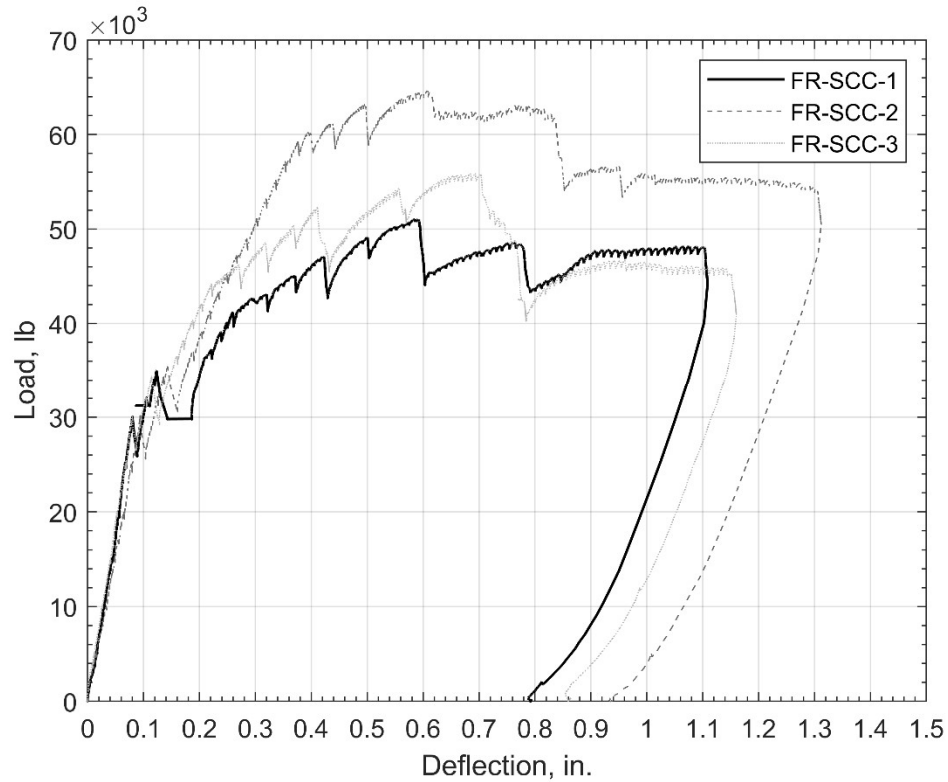
Figure 4.23: Load vs. Deflection Curves of FR-SCC Girders

4.3.3 UHPC Girders

4.3.3.1 UHPC-1 Girder

4.3.3.1.1 Overview

The cracking pattern at failure for girder UHPC-1 and associated load marks are shown in Figure 4.22. As shown in this figure, the initial crack was a web shear crack that appeared in the web as the load reached 35 kips. As additional load was applied the crack propagated upward and downward diagonally. A few additional shear cracks appeared and spread as the load increased. Flexural cracks appeared underneath the loading point and closer to the middle of the girder. The primary crack was the flexure shear crack observed beginning at the bottom flange of the girder between the load point and repaired region when the load approached 35 kips.

Figure 4.24: UHPC-1 Girder after Test with SW Side (Left) and SE Side (Right)

4.3.3.1.2 Load vs. Deflection Behavior of UHPC-1 Girder

Figure 4.23 shows the load vs. deflection behavior of the UHPC-1 girder compared to the load vs. deflection curves for reference undamaged reference beams M1-U and M3-U. The UHPC-1 girder had a peak load of 78 kips and 1.1 in. deflection, which was 44 percent greater than the upper bound M3-U girder. There was a noticeable increase in both load and deflection for the UHPC-1 girder after the first crack occurred at a load of 35 kips. Between applied loads of 28 kips and 48 kips, the UHPC-1 girder's deflection behavior was very similar to the deflection of girder M1-U under the same loads while the stiffness of girder M3-U was larger in that range. Beyond 48 kips of load, UHPC-1 surpassed the two undamaged reference beams in terms of both load and deflection. The measured capacity of UHPC-1 was also higher than the estimated capacity calculated in Appendix 7.3 for flexural capacity, but less than the shear capacity calculated in Appendix 7.4.
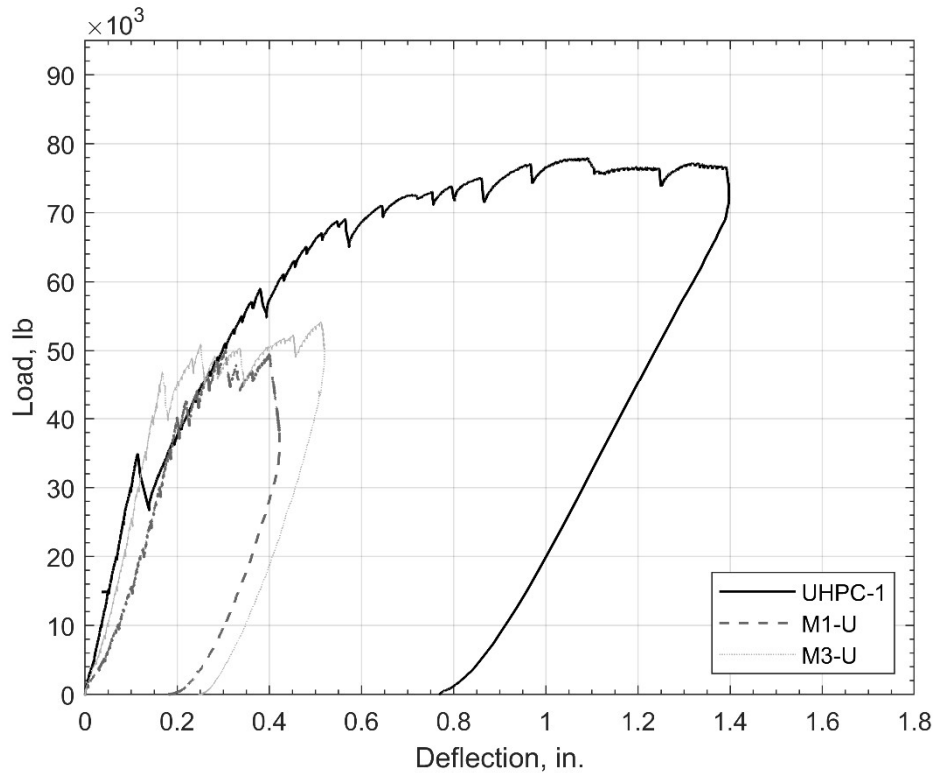
Figure 4.25: Load vs. Deflection Curves of UHPC-1 Girder and Undamaged Reference Beams

4.3.3.1.3 Load vs. Slip Behavior and Failure Mechanism of UHPC-1 Girder

The load vs. slip behavior of the UHPC-1 girder is shown in Figure 4.24 along with the load vs. deflection curve. The slip data of UHPC-1 girder was stopped before the end of the test because the LVDTs run out of measurement range. The strands started slipping at approximately 59 kips, which was significantly larger than the first cracking load of 35 kips. After the first crack, the stiffness of the girder was reduced greatly, but it was still significantly larger than the stiffness after the first slip was observed. In addition, the cracks propagated diagonally in both directions and disturbed the strands as load gradually increased, which caused strand slip. Based on the crack pattern from Figure 4.22, slip behavior, load vs. deflection behavior and the failure mechanism, the failure type of this girder was classified as bond-shear/flexure based on Naji et al. (2016).

73
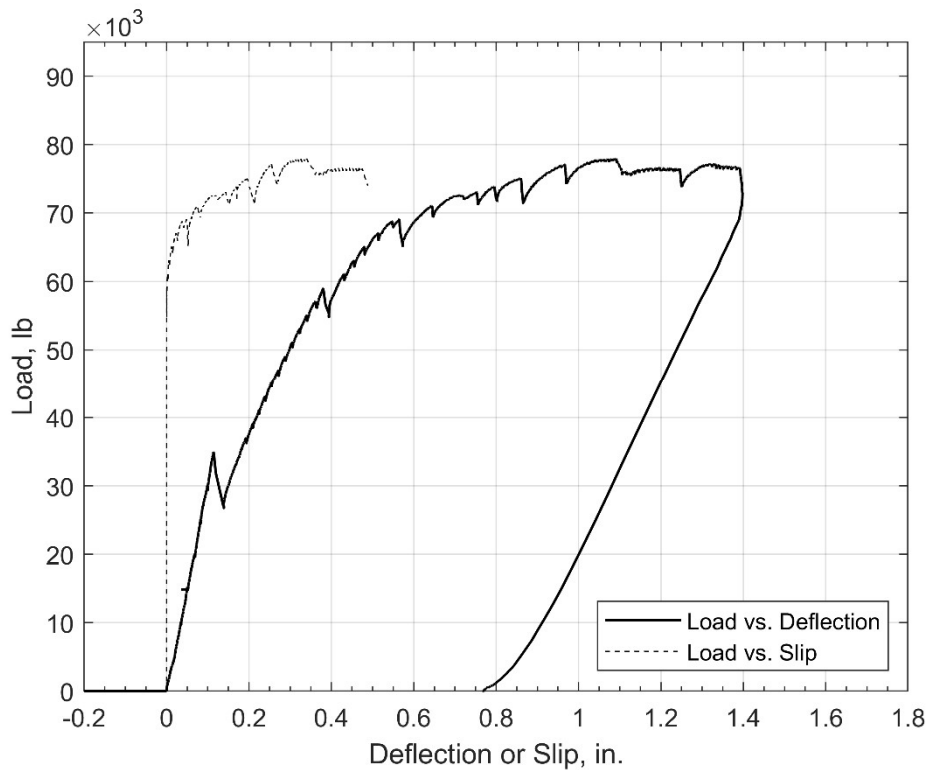
Figure 4.26: Load vs. Deflection and Load vs. Slip Curves of UHPC-1 Girder

4.3.3.2 UHPC-2 Girder

4.3.3.2.1 Overview

Figures 4.25 and 4.26 show the cracking pattern at failure on both sides of the UHPC-2 girder and the minor crack at the junction between the girder and UHPC repair material at the bottom surface. The first crack, which was a nearly vertical flexural crack, occurred beginning at the bottom flange and extending into the web under the loading point of this girder at a load of 43 kips. Several shear cracks occurred close to the support as the load increased, and these shear cracks dispersed into branches that propagated toward the loading point. When the load exceeded 51 kips, there was the first appearance of a flexural crack located under the loading point. As

74

load increased, other flexure/flexure-shear cracks occurred and propagated at the middle of the girder on both sides.

Figure 4.27: UHPC-2 Girder after Test with SW Side (Left) and SE Side (Right)

Figure 4.28: Cracks in Bottom Flange of UHPC-2 Girder after Test

4.3.3.2.2 Load vs. Deflection Behavior of UHPC-2 Girder

At a load of 43 kips, the first wide crack occurred, which caused the first drop in the load vs. deflection curve shown in Figure 4.27. Although the initial cracking load of the UHPC-2

75

girder was lower than for the two undamaged reference beams, its ultimate strength was much

higher as it reached 88.7 kips at 1.48 in. of deflection as compared to M3-U (54 kips, 0.51 in.)

and M1-U (50 kips, 0.305 in.). After the first crack, the stiffness of the girder decreased

significantly as the deflection increased greatly compared with the gradual increase of the load.

The load plateau visible in Figure 4.27 indicated yielding of the reinforcement. The measured

capacity of the UHPC-2 girder surpassed both the estimated flexural capacity and shear capacity

computed in Appendix 7.3 and 7.4.

Figure 4.29: Load vs. Deflection Curves of UHPC-2 Girder and Undamaged Reference Beams

4.3.3.2.3 Load vs. Slip Behavior and Failure Mechanism of UHPC-2 Girder

The load vs. slip curve is shown in Figure 4.28 along with the load vs. deflection curve for specimen UHPC-2. The slip data of UHPC-2 girder was stopped before completion of the test because the LVDTs ran out of measurement range. As shown in this Figure, the prestressing strand started slipping at approximately 69 kips of load, which was much higher than the initial cracking load of 43 kips. As shown in Figure 4.28, the strand exhibited only just more than 0.2 in. of slip before failure, which is less than observed for the other repair materials (except for the MALP-1 girder, which exhibited no prestressing strand slip). Based on the crack pattern and load vs. slip curve with crushing the deck, the failure type was determined as bond-shear/flexure based on Naji et al. (2016).
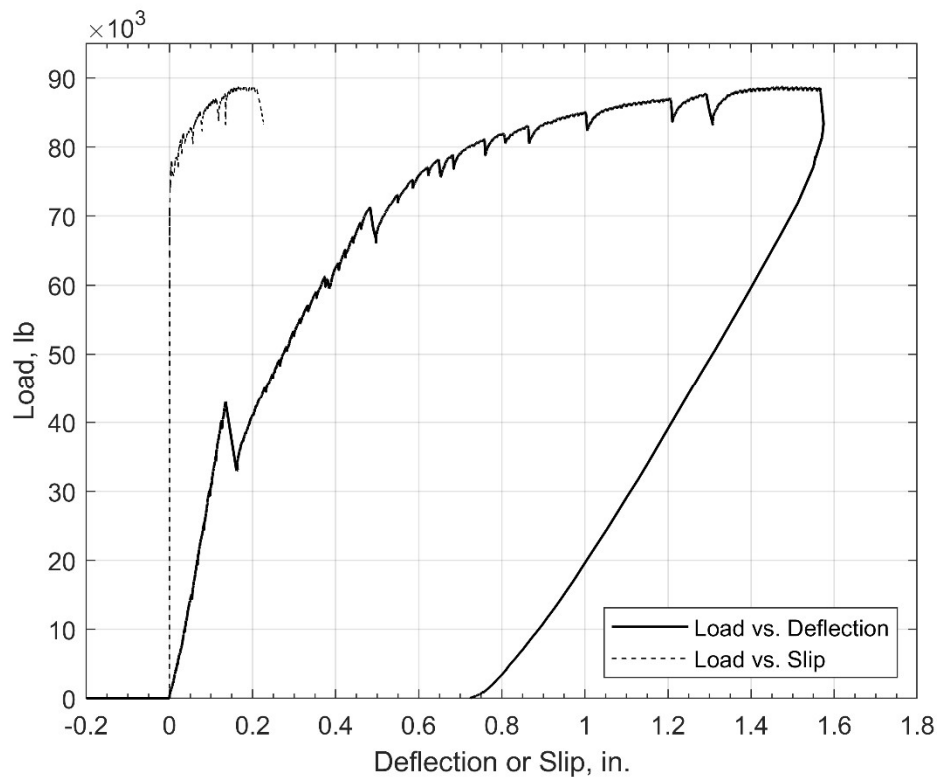
Figure 4.30: Load vs. Deflection and Load vs. Slip Curves of UHPC-2 Girder

77

4.3.3.3 UHPC-3 Girder

4.3.3.3.1 Overview

Figure 4.29 shows the cracking pattern and associated loading marks for the UHPC-3 girder after testing. The initial crack was a web shear crack that appeared in the web of the girder at a load of 34 kips. As load increased, the initial crack propagated diagonally upward and downward coinciding with new shear cracks and flexural cracks. Flexural cracks appeared at the bottom flange under the loading point at 52 kips, and in the middle of the girder at approximately 74 kips and 86 kips. The widest cracks at failure were the flexural cracks beneath the load point and the concrete crushed in the deck at failure, both of which are indicative of a flexural failure.

Figure 4.31: UHPC-3 Girder after Test with SE Side (Left) and SW Side (Right)

4.3.3.3.2 Load vs. Deflection Behavior of UHPC-3 Girder

The load vs. deflection curve for girder UHPC-3 is shown in Figure 4.30 along with curves for reference undamaged reference beams M1-U and M3-U. As shown in Figure 4.30, the UHPC-3 girder had a peak load of 89.5 kips and 1.61 in. maximum deflection. The UHPC-3

girder had an earlier first crack at 34 kips as compared to M1-U (40 kips) and M3-U (47 kips). However, the load increased significantly after the first crack, which was not the case for the undamaged reference beams. Furthermore, the measured capacity of the UHPC-3 girder surpassed the flexural capacity and shear capacity estimated in Appendix 7.3 and 7.4.

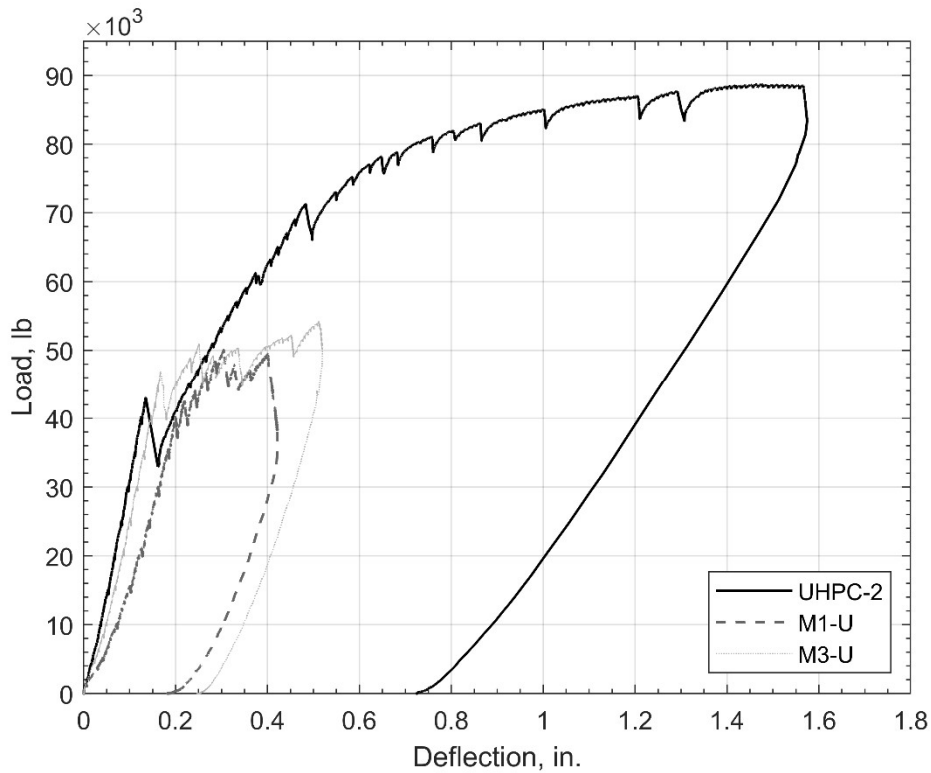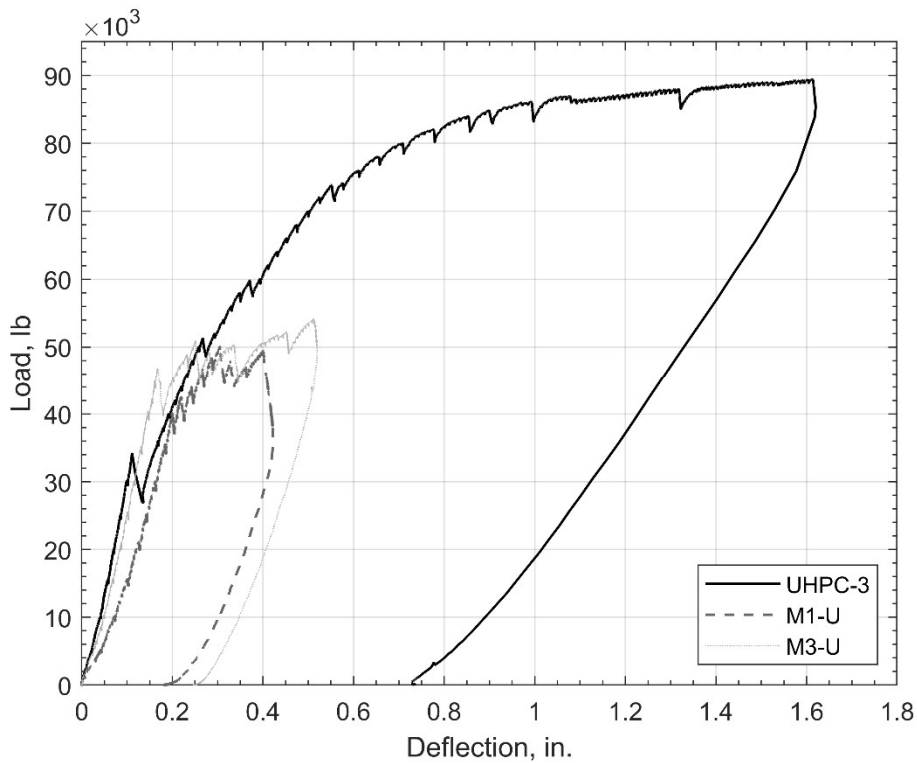**Figure 4.32:** Load vs. Deflection Curves of UHPC-3 Girder and Undamaged Reference Beams

4.3.3.3.3 Load vs. Slip Behavior and Failure Mechanism of UHPC-3 Girder

The load vs. slip curve for the UHPC-3 girder is shown in Figure 4.31 along with the load vs. deflection curve. The first strand slip was measured at a load 86.1 kips. There was only 0.00344 in. of strand slip measured as the maximum load of 89.5 kips was reached. The maximum slip magnitude that the strands reached was recorded at 0.00455 in. at 85.5 kips. The load at strand slipping was much higher than the initial cracking load (34 kips) and the yielding

79

plateau shape of the load vs. deflection curve was more indicative of a flexural failure. Combining high loading at first strand slip and crack pattern, the failure mechanism of UHPC-3 girder was bond-shear/flexure based on the criteria of Naji et al. (2016).
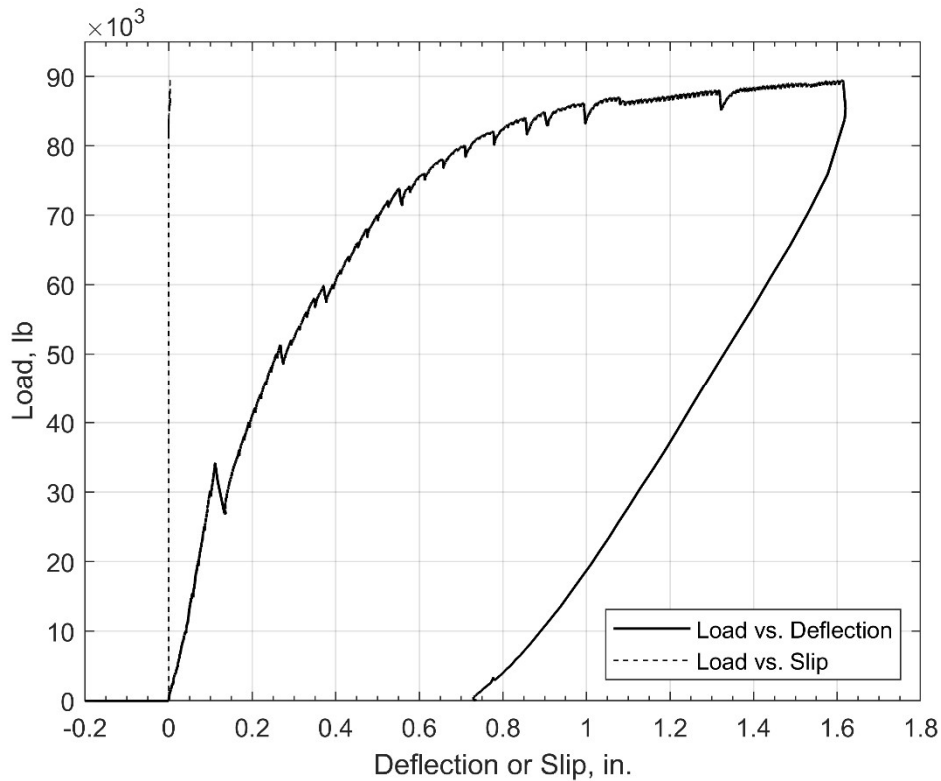
Figure 4.33: Load vs. Deflection and Load vs. Slip Curves of UHPC-3 Girder

4.3.3.4 Summary of UHPC Girder Tests

In general, the UHPC repaired girders had higher ultimate loads and deflections compared to the undamaged reference beams. For deflection, the measured deflection of the UHPC repaired specimens indicated very ductile behavior in addition to improved load carrying capacity. For strand slip, the prestressing strand started slipping at higher load compared to the initial crack indicating that first slip was not a result of a crack through the anchorage zone. The

UHPC repair played an outstanding role as a large anchorage that was bonding to the original girder and strands very well. Figure 4.34 shows that all three girders exhibited very similar behavior other than the smaller ultimate load for specimen UHPC-1.
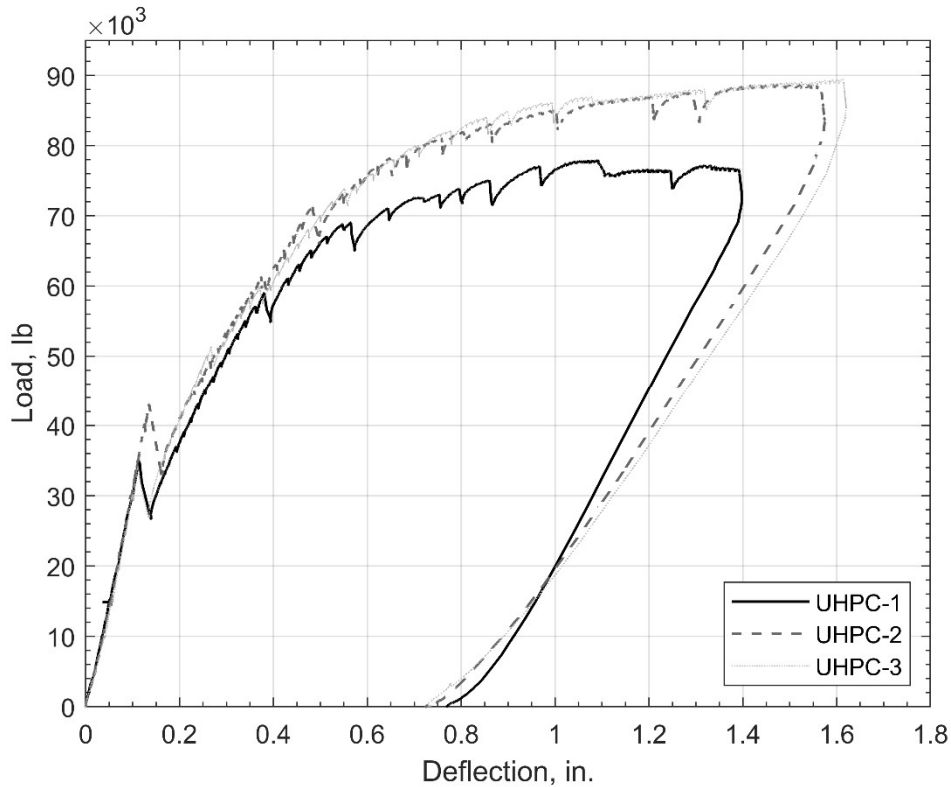
Figure 4.34: Load vs. Deflection Curves of UHPC Girders

4.4 Result Summary

Figure 4.35 shows the average peak load and deflection from the repaired girder tests. The MALP repaired girders had the lowest average peak load of 44 kips with the medium average deflection of 0.73 in. The FR-SCC repaired girders had the medium average peak load of 57.2 kips corresponding with the lowest average deflection of 0.63 in. Compared to other

repaired girders, UHPC had the highest values in both average peak load and deflection, 85.4 kips and 1.40 in, respectively.
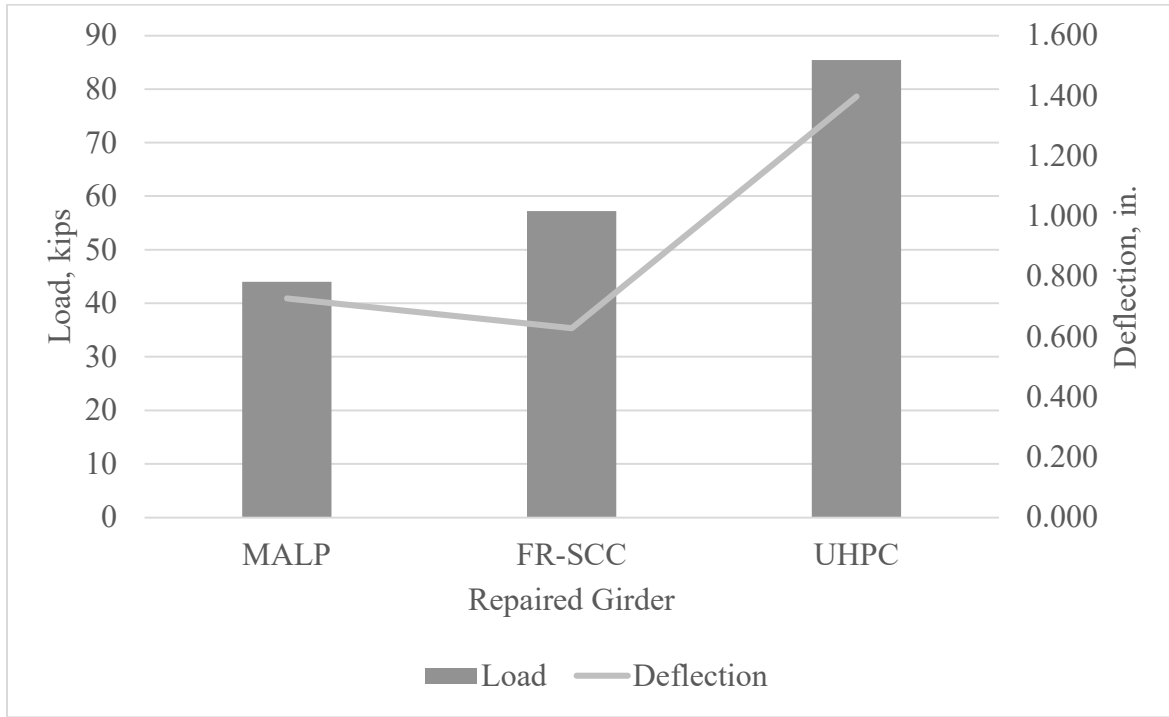
Figure 4.35: Average Peak Loads and Average Deflection at Peak Loads of Repaired Girders

A comparison of the results from the repair beam tests to the two reference undamaged reference beams is presented in Table 4.3 and Figure 4.36.

Table 4.3: Percentage Difference of Cracking Loads and Peak Loads of Repaired Girders Compared to Undamaged Reference Beams

Repair Material	Beam Test Number	Cracking Load, kips	Peak Load, kips	M1-U (Lower Bound) Percentage Difference		M3-U (Upper Bound) Percentage Difference	
				Cracking Load	Peak Load	Cracking Load	Peak Load
MALP	1	35	43	-12.5	-14	-25.5	-20.4
	2	37	42.6	-7.5	-14.8	-21.3	-21.1

	3	30	46.4	-25	-7.2	-36.2	-14.1
FR-SCC	1	30	51	-25	2	-36.2	-5.6
	2	30	64.6	-25	29.2	-36.2	19.6
	3	30	56	-25	12	-36.2	3.7
UHPC	1	35	78	-12.5	56	-25.5	44.4
	2	43	88.7	7.5	77.4	-8.5	64.3
	3	34	89.5	-15	79	-27.7	65.7

The lower bound M1-U beam had a cracking load of 40 kips and an ultimate load of 50 kips while the upper bound M3-U beam had a cracking load of 47 kips and an ultimate load of 57 kips, but tests of both beams were artificially stopped to achieve the specific failure state. While the beams had likely reached their peak loads, they could have been pushed to additional deflection. Figure 4.33 shows the average cracking load and peak loads of the repaired beams associated with the undamaged reference beams. As compared to the M1-U beam (lower bound), the difference in cracking load ranges from -25% to 7.5% while the difference in peak load ranges from -14.8% to 79%. Compared to the M3-U beam (upper bound), the cracking load difference was in range from -36.2% to -8.5% while the difference in peak load ranged from -20.4% to 65.7%. The result indicated that all repaired girders had moderately low cracking loads compared to the undamaged reference beams. The explanation for this issue comes from the fact that the loading point of the simulated corroded beam was in transfer length region as the effective length of the girders to transfer prestress was shortened by 18 inches due to the induced damage. The contribution of prestress force to the cracking resistance was also reduced by the same effect. On the contrary, the peak load was increased significantly for the UHPC repair girders and slightly for the FR-SCC repair girders. This outcome showed that UHPC and FR-SCC played important role as a strong anchorage and support to resist loads. However, for the MALP repair beams all cracking loads and peak loads were much less than those for the M1-U

(lower bound) beam. There were several explanations for the MALP repair performance. First of all, the MALP repair material did not appear to bond well to the prestressing strand and the conventional concrete. The second explanation was due to the MALP material's characteristics which included a very fast set; the MALP material almost set when pouring into the repair forms and produced several individual layers. Therefore, the performance of the repair materials in the girder specimens followed trends as the repair materials performed in the two bond tests, in which UHPC and FR-SCC were dominant repair materials with high strength and better bonding compared to low strength and weak bonding of the MALP material.
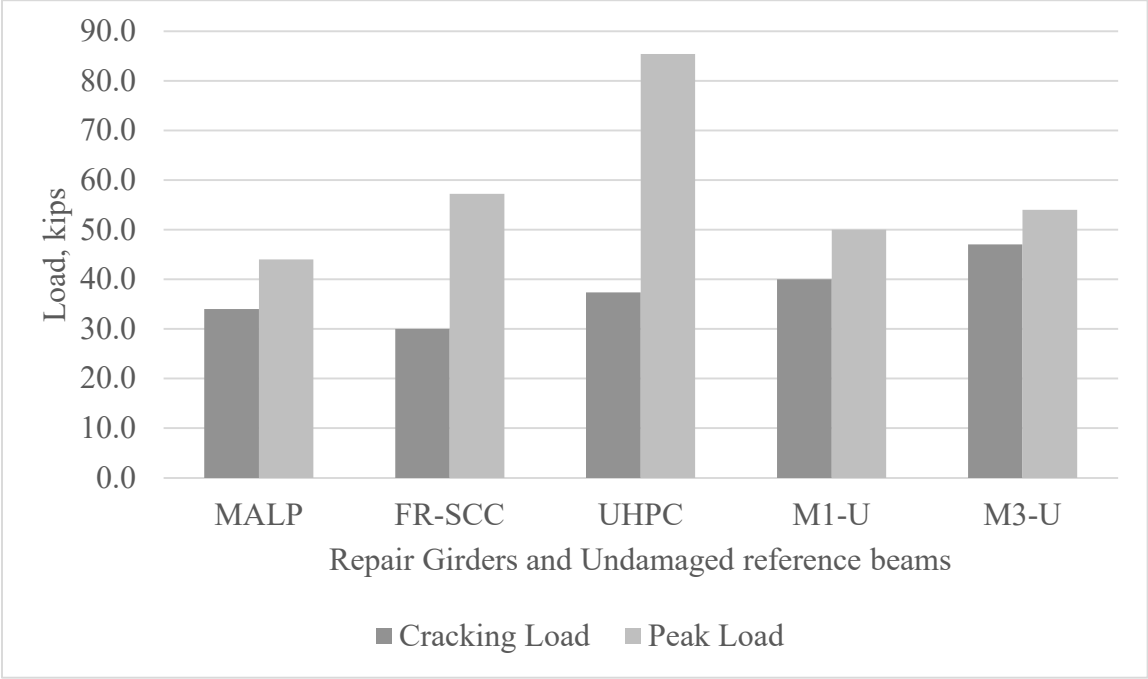

Figure 4.36: Average Cracking Loads and Average Peak Loads of Repaired Girders and Undamaged Reference Beams

Chapter 5 Conclusions and Recommendations

5.1 Summary

The primary goal of this research was to establish and identify a functional technique to restore the lost shear capacity in precast prestressed concrete girders damaged by corrosion in the end regions and to protect the girder from future deterioration using innovative concrete materials. A secondary goal was to identify a testing technique for quality assurance for bond of the repair materials to the girder concrete. The first goal was addressed by constructing and testing half-scale AASHTO Type II girders with induced damage, repairing the girders with three innovative concrete materials, determining the strength of girders after applying repaired materials through load testing, and comparing the girder load test results with similar data from tests of undamaged reference beams and analytical values. The ultimate strengths of repaired girders were compared in helping decide the best repair materials for a specific application. Detailed calculations presented in Appendix were used to evaluate whether the repairs restored capacity of the girders. In addition, for the second goal the bond test results provided a general indication about not only the bond strength between the repair materials and the conventional concrete under compression and tension, but also prediction about the failure mechanism for each type of repair material. A summary of the conclusions and recommendations is given in the following sections.

5.2 Conclusions

- Experimental results indicated that a 4% - 65% improvement in the girders' maximum capacity with extended ductility compared to the original beam behavior could be achieved with the UHPC and FR-SCC repairs. However, the girders repaired with MALP

concrete gave ultimate loads that were much lower than for the undamaged reference beams M1-U and M4-U.

- The repair materials changed the failure mechanism of most girders, except for the MALP-1 girder which did not change its failure mechanism, from a bond-shear failure mechanism in the original beams to a more ductile bond-shear/flexure failure. This new failure mechanism gave noticeable deflections at maximum capacity of the girders before the deck crushed at the load point. This result indicates that the repair materials can change the failure mechanism of tested girders and improve the overall girder behavior even if the prestress is lost or not originally present in the end region of the girder.

- The UHPC repair exhibited better performance in comparison with the FR-SCC and MALP repairs in terms of cracking, strand slip, deflection, and ultimate loads despite having a smaller minimum repair thickness. In addition, the 2% of steel fibers in UHPC executed a better bonding between the repair and the strands that provided a great anchorage, which prevented strands slipping during testing. This result reveals the relationship between the repair materials' components, efficiency, compressive strength, and overall performance as a repair. However, FR-SCC repair performed well in rehabilitating the corroded end region of the girders, shown by increasing the girders' capacity.

- During this research, the UHPC repair material had an advantage over the FR-SCC repair as the UHPC used dried sand while FR-SCC repair used materials that contained surface moisture, which required a water content adjustment for each batch. Therefore, the UHPC workability was more consistent than that of the FR-SCC, but this can be accounted for with proper experience.

- In most cases, the first crack occurred before the strands started slipping, which indicates the repair material acted as a strongly bonding anchorage that prevented the prestressing strand from slipping and the repair may have contributed to shear resistance of the girder.

- Based on the results of this research, both the splitting tensile test and slant shear test had the same trends as the larger repair experiments relative to repair material performance. UHPC had the highest bond strength followed by the FR-SCC and then the MALP had the lowest strength of all three repairs for both the bond test and structural testing.

5.3 Recommendations

- In this research, the load point was located 3.5 ft away from the end of the tested girders, which resulted in an a/d <2.5. Further research on performance of end region repairs with different point load locations is recommended, in which the ratio a/d should be less than 4.5 for near support or end region behavior as described by Naji et al. (2016).

- Based on the performance of UHPC and FR-SCC in this research, they are considered to be the best options of those considered for repairing and boosting the service and ultimate state of girders damaged at the end regions.

- It would likely be better to encapsulate more of the damaged region than done in this research for all repair materials to further strengthen the girders' capacity and prevent a crack occurring at the junction of the repairs and the girders. However, further research is required to prove this claim and optimize the dimensions of the repairs, since the applied load in this testing was only placed 3.5 ft away from the end of the girders.

- For this research, the corroded region was represented by keeping a hollow space at the bottom flange of the girder and casting repair materials to restore the girder's capacity and protect the reinforcement. Further research is required to examine the behavior of

girders with actual corrosion damage including spalled concrete and prestressing strand damage.

- The cause of the reduced performance of the MALP repairs should be considered for further research. The MALP is quick hardening material and easily affected by the ambient temperature. Therefore, it loses its workability quickly after blending due to the exothermic reaction between the powder and activator, which leads to challenges in construction in hot weather and may have partially led to the poor performance in this research.

- MALP's advantage comes from is fast set when repairs must be done quickly, however further research on MALP concrete should be conducted to ensure this material has appropriate workability for use in structural applications.

- Although both bond tests showed considerable potential in predicting the bond and failure mechanisms between repair materials and the conventional concrete, more experiments are needed to verify the consistency and accuracy of results, especially for the slant shear test.

- Strand slip should be measured at both the end of the beam and where the repair meets the rest of the beam to evaluate the relationship between cracks, prestress force, and strand slip for prestressed bridge girders.

- Finally, further research is needed on how behavior of the repair materials plays a role as an anchorage of prestressed girders in relationship with bond behavior at the corroded region.

Chapter 6 References

AASHTO LRFD Bridge Design Specification. (2017). Washington, DC: American Association of State Highway and Transportation Officials.

Abosrra, L., Ashour, A., & Youseffi, M. (2011). Corrosion of Steel Reinforcement in Concrete of Different Compressive Strengths. *Construction and Building Materials, 25*, 3915-3925. doi:10.1016/j.conbuildmat.2011.04.023

ACI 318-14: Building Code Requirements for Structural Concrete. (2014). Farmington Hills, MI: American Concrete Institue.

Ahmadi, M. (2021). *End Regions Repair of Prestressed Girders for Restoring the Shear Capacity Using UHPC, FR-SCC, and MALP.* University of Oklahoma.

ASTM C1611/C1611M-21 Standard Test Method for Slump Flow of Self-Consolidating Concrete. (2021). West Conshohocken, PA, United States. doi:10.1520/C1611_C1611M-21

ASTM C496/C496M-17 Standard Test Method for Splitting Tensile Strength of Cylindrical Concrete Specimens. (2017). West Conshohocken, PA, United States. doi:10.1520/C0496_C0496M-17

ASTM C882/C882M-20 Standard Test Method for Bond Strength of Epoxy-Resin Systems Used with Concrete by Slant Shear. (2020). West Conshohocken, PA, United States. doi:10.1520/C0882_C0882M-20

Bruce, S., McCarten, P., Freitag, S., & Hasson, L. (2008). *Deterioration of Prestressed Concrete Bridge Beams.* Welington: Land Transport New Zealand. Retrieved from http://www.landtransport.govt.nz/research/reports/337.pdf

Casey, C. W. (2019). *Ultra-High Performance Concrete for Connections of Precast, Prestressed Girders Made Continuous for Live Load.* Master Thesis, University of Oklahoma, Civil Engineering and Environmental Science, Norman.

Choate, J. (2018, August 02). *Implementing Fiber-Reinforced Self-Consolidating Concrete as a Repair Material for AASHTO Prestressed Concrete Girders.* Master Thesis, University of Oklahoma, School of Civil Engineering and Environmental Science, Norman. Retrieved March 20, 2020

Coleman, R. (2018). *Comparative Study of Surface Preparation and Bond Angle Combinations for Bridge Repair Using Ultra-High Performance Concrete Alternative.* Master Thesis, University of Oklahoma, Civil Engineering and Environmental Science, Norman.

Day, R. (1994). Strength Measurement of Concrete Using Different Cylinder Sizes: A Statistical Analysic. *American Society for Testing and Materials*, 21-30.

Dinges, T. (2009). *The History Of Prestressed Concrete: 1888 To 1963*. Manhattan: Kansas State University.

Federal Highway Administration. (2005, December). Advances in Self-Consolidating Concrete. Washington, District of Columbia, United States of America: Federal Highway Administration. Retrieved from https://www.fhwa.dot.gov/publications/focus/05nov/01.cfm

Federal Highway Administration. (2013). Retrieved from Bridge by Year Built, Year Reconstructed and Material Type 2013: https://www.fhwa.dot.gov/bridge/nbi/no10/yrblt_yrreconst13.cfm

Federal Highway Administration. (2018, December 31). Bridge Condition by Highway System 2018. Washington, District of Columbia, United States of America. Retrieved from https://www.fhwa.dot.gov/bridge/nbi/no10/condition18.cfm

Floyd, R. W., Volz, J. S., Looney, T., Mesigh, M., Ahmadi, M., Roswurm, S., . . . Huynh, P. (2021). *Evaluation of Ultra-High Performance Concrete, Fiber Reinforced Self-Consolidating Concrete, and MALP Concrete for Pretressed Girder Repair*. Oklahoma City: Oklahoma Department of Transportation.

Funderburg, C. (2018). *Evaluation of Surface Preparation and Bond Angle Combinations for Joint Replacement Using Ultra-High Performance Concrete*. Master Thesis, University of Oklahoma, Civil Engineering and Environmental Science, Norman.

Graybeal, B. (2016). *Bond of Field-Cast Grout to Precast Concrete Elements*. McLean: Federal Highway Administration.

Graybeal, B. A. (2006). *Material Property Characterization of Ultra-High Performance Concrete*. United States: McLean, VA: Federal Highway Administration, Office of Research, Development and Technolgy, Turner-Fairbank Highway Research Center.

Graybeal, B. A. (2011, March). Ultra-High Performance Concrete. Washington, DC, United States. Retrieved from U.S. Department of Transportation Federal Highway Administration: https://www.fhwa.dot.gov/publications/research/infrastructure/structures/11038/index.cfm

Graybeal, B. A. (2014, March 08). Splice Length of Prestressing Strands in Field-Cast UHPC Connections. *Materials and Structures, 48(6)*, 1831-1839. doi:10.1617/s11527-014-0277-8

Guettala, A., & Abibsi, A. (2006, June 08). Corrosion Degradation and Repair of A Concrete Bridge. *Materials and Structures, 39*, 471-478. doi:https://doi-org.ezproxy.lib.ou.edu/10.1007/s11527-005-9046-z

(2017). *Infrastructure Report Card*. Reston: ASCE.

Kassimi, F. (2013). Development and Performance of Fiber-Reinforced Self-Consolidating Concrete for Repair Applications. ProQuest.

Kusumawardaningsih, Y., Fehling, E., Ismail, M., & Aboubakr, A. (2015). Tensile Strength Behavior of UHPC and UHPFRC. *The 5th International Conference of Euro Asia Civil Engineering Forum. 125*, pp. 1081-1086. Elsevier. doi:10.1016/j.proeng.2015.11.166

Mayhorn, D. (2016, August 09). *Investigation of the Effect of End Region Deterioration in Precast, Prestressed Concrete Bridge Girders.* Master Thesis, University of Oklahoma, School of Civil Engineering and Environmental Science, Norman.

McDaniel, A. S. (2017). *Development of Non-Proprietary Ultra-High Performance Concrete Mix Designs.* Master Thesis, University of Oklahoma, Civil Engineering and Environmental Science, Norman.

Mesigh, D. (2021). *Evaluation of Specialized Concretes for the Repair of Damaged Continuity Joints in Prestressed Girder Bridges.* Master Thesis, University of Oklahoma, Department of Civil Engineering and Environmental Science, Norman.

Naji, B., Ross, B. E., & Floyd, R. W. (2016). Characterization of Bond-Loss Failures in Pretensioned Concrete Girders. *Journal of Bridge Engieering, 22(4)*.

PCI Design Handbook (7th ed.). (n.d.).

Phoscrete. (n.d.). Retrieved from Technical: https://www.phoscrete.com/data-guides/

Szilard, R. (1969). Corrosion and Corrosion Protection of Tendons in Prestressed Concrete Bridges. *ACI Journal, 66(1)*, 42-59.

Wirkman, C. (2016). *Performance of Fiber-Reinforced Self-Consolidating Concrete for Repair of Bridge Sub-Structure.* Master Thesis, University of Oklahoma, Civil Engineering and Environmental Science, Norman.

Yee, A. A. (1976). Prestressed Concrete for Buildings. *PCI Journal*, 112-157. Retrieved from https://doi.org/10.15554/pcij.09011976.112-157

Zmetra, K. (2015, April 17). *Repair of Corrosion Damaged Steel Bridge Girder Ends by Encasement in Ultra-High Strength Concrete.* Hartford: University of Connecticut. Retrieved March 29, 2020

Chapter 7 Appendix

7.1 Notation and Terminology

a =   depth of equivalent rectangular stress block, in.

A_{ct} =   area of concrete on the flexural tension side of the member, in.^{2}

A_g =   gross area of concrete section, in.^{2}

A_{ps} =   area of prestressing reinforcement, in.^{2}

A_s =   area of nonprestressed tension reinforcement, in.^{2}

A'_s =   area of nonprestressed compression reinforcement, in.^{2}

A_{tr} =   area of transformed section, in.^{2}

A_v =   area of shear reinforcement within spacing s, in.^{2}

b =   width of compression face of member, in.

b_d =   width of the deck, in.

b_v =   effective web width taken as the minimum web due to flexure, in.

C =   total compression force, kips

c =   distance from extreme compression fiber to neutral axis, in.

d =   distance from extreme compression fiber to centroid of longitudinal tension

reinforcement, in.

d' =   distance from extreme compression fiber to centroid of longitudinal compression

reinforcement, in.

d_e = effective depth from extreme compression fiber to the centroid of the tensile force in the tensile reinforcement, in.

d_p = distance from extreme compression fiber to centroid of prestressing reinforcement, in.

d_v = effective shear depth taken as the distance from the extreme compression fiber, in.

E_c = modulus of elasticity of concrete, ksi

E_{ci} = modulus of elasticity of concrete at transfer, ksi

E_p = modulus of elasticity of prestressing reinforcement, ksi

E_s = modulus of elasticity of steel reinforcement, ksi

e_{tr} = eccentricity of prestressing strands with respect to centroid of composite member, in.

f'_c = compressive strength of concrete at 28 days, ksi

f_{cgp} = compressive stress of prestressing strand due to the prestressing force immediately at transfer and the self-weight of the member at the section of maximum moment, ksi

f'_{ci} = compressive strength of concrete at time of initial prestress, ksi

f_{pi} = prestressing steel stress immediately prior to transfer, ksi

f_{ps} = stress in prestressing reinforcement at nominal flexural strength, ksi

f_{pu} = tensile strength of prestressing reinforcement, ksi

f_{py} = yield strength of prestressing reinforcement, ksi

f_s = tensile stress in nonprestressed reinforcement, ksi

f'_s = compressive stress in nonprestressed reinforcement, ksi

f_{se} = effective stress in prestressing reinforcement after losses, ksi

f_y = yield strength of nonprestressed reinforcement, ksi

H = average annual ambient relative humidity, percent

h = overall depth of member, in.

I_g = moment of inertia of gross concrete section about centroidal axis, neglecting the reinforcement, in.^{4}

I_{tr} = moment of inertia of transformed composite section about centroidal axis, including the reinforcement, in.^{4}

K_1 = correction factor for source of aggregate to be taken as 1.0 unless determined by physical test, and as approved by the owner

L = span length, ft

M_0 = unfactored moment caused by self-weight of the member, k-ft

M_n = nominal flexural strength at section, k-ft

M_u = factored moment at section, k-ft

n_i = modular ratio between concrete and reinforcement

P_i = load transfer to prestressing reinforcement at prestress, kips

s = center-to-center spacing of transverse reinforcement, in.

s_{max} = maximum permitted spacing of transverse reinforcement, in.

T = total tension force, kips

94

V_C = nominal shear resistance of the concrete, kips

V_S = shear resistance provided by transverse reinforcement, kips

V_u = factored shear load, kips

v_u = shear stress, ksi

w_C = unit weight of concrete, kcf

w_0 = weight of member, k/ft

y_b = distance from centroid axis of gross section, neglecting reinforcement, to bottom of member, in.

y_{tr} = distance from centroid axis of the transformed composite section to bottom of member, in.

α = angle of inclination of transverse reinforcement to longitudinal axis, degrees

β_1 = factor relating depth of equivalent rectangular compressive stress block to depth of the neutral axis

γ_h = correction factor for relative humidity of the ambient air

γ_{st} = correction factor for specified concrete strength at time of prestress transfer to the concrete member

Δf_{pES} = losses due to elastic shortening at the time of application of prestress, ksi

Δf_{pLT} = losses due to long-term shrinkage and creep of concrete, and relaxation of the prestressing steel, ksi

Δf_{pR} = estimate of relaxation loss at final time taken as 2.4 ksi for low relaxation strand

Δf_{pT} = total prestress losses, ksi

ε_{ps} = strain of prestressing reinforcement at nominal strength, in./in.

ε_s = strain of tension reinforcement at nominal strength, in./in.

ε'_s = strain of compression reinforcement at nominal strength, in./in.

λ = concrete density modification factor

ϕ = resistance factor

7.2 Prestress Loss Calculation Based on AASHTO LRFD Method (Approximate Method)

The purpose of this calculation is to determine the prestress loss of the girder and resulting effective prestress. The effective prestress will be used along with the transfer length and development length to check whether the load point was in range of transfer length and resulting effects on shear capacity. For this purpose, a spreadsheet was developed using the Approximate Method described in AASHTO LRFD (2017). To explain how the spreadsheet worked, the calculation is presented as follows:

Input data:

$A_g = 105.75$ in.^{2}

$I_g = 5873.8$ in.^{4}

$y_b = 9.968$ in. $\qquad\qquad\qquad\qquad\qquad w_u = 0.11$ k/ft

$w_c = 0.15$ kcf $f'_c = 7$ ksi

$f'_{ci} = 4$ ksi $L = 16.5$ ft

$A_{ps} = 0.334$ in.^{2} $E_p = 28,500$ ksi

$f_{pu} = 270$ ksi $f_{py} = 243$ ksi

$f_{pi} = 202.5$ ksi $K_1 = 1.0$

$H = 63\%$ $\Delta f_{pR} = 2.4$ ksi

Require: Calculate the prestress loss of the girder

a) Transformed Section

$$E_{ci} = 33,000K_1 w_c^{1.5}\sqrt{f'_{ci}} = 33,000(1.0)(0.15\ kcf)^{1.5}\sqrt{4\ ksi} = 3834.3\ ksi$$

$$n_i = \frac{E_p}{E_{ci}} = \frac{28,500\ ksi}{3834.3\ ksi} = 7.433$$

$$A_{tr} = A_g + (n_i - 1)A_{ps} = 105.75\ in.^2 + (7.433 - 1)(0.334\ in.^2\ ) = 107.9\ in.^2$$

$$y_{tr} = \frac{\Sigma Ay}{A} = \frac{105.75\ in.^2\ (9.957\ in) + (7.433 - 1)(0.334\ in.^2\ )(2\ in.\ )}{107.9\ in.^2} = 9.809\ in.$$

$$e_{tr} = y_{tr} - y_s = 9.809\ in. - 2.0\ in. = 7.809\ in.$$

$$I_{tr} = I_g + A_g d_g^2 + A_{ps} d_{ps}^2$$

$$= 5873.8\ in.^4 + (105.75\ in.^2\ )(9.968\ in. - 9.809\ in.\ )^2$$

$$+ (7.433 - 1)(0.334\ in.^2\ )(9.809\ in. - 2.0\ in.\ )^2 = 6007.5\ in.^4$$

b) Elastic Shortening

$$P_i = A_{ps}f_{pi} = (0.334 \ in.^2)(202.5 \ ksi) = 67.635 \ kips$$

$$M_0 = \frac{w_0L^2}{8} = \frac{\left(0.11\frac{k}{ft}\right)(16.5ft)^2\left(12\frac{in.}{ft}\right)}{8} = 44.985 \ k.-in$$

$$f_{cgp} = -\frac{P_i}{A_{tr}} - \frac{P_ie_{tr}^2}{I_{tr}} + \frac{M_0e_{tr}}{I_{tr}}$$

$$= -\frac{67.635 \ ksi}{107.9 \ in.^2} - \frac{(67.635 \ ksi)(7.809 \ in.)^2}{6007.5 \ in.^4} + \frac{(44.985 \ k.in)(7.809 \ in.)}{6007.5 \ in.^4}$$

$$= -1.255 \ ksi$$

$$\Delta f_{pES} = \frac{E_p}{E_{ci}}f_{cgp} = \frac{28,500 \ ksi}{3834.3 \ ksi}(1.255 \ ksi) = 9.33 \ ksi$$

c) Long-term Loss

$$\gamma_h = 1.7 - 0.01H = 1.7 - 0.01(63\%) = 1.07$$

$$\gamma_{st} = \frac{5}{1 + f_{ci}'} = \frac{5}{1 + 4 \ ksi} = 1$$

$$\Delta f_{pLT} = 10\frac{f_{pi}A_{ps}}{A_g}\gamma_h\gamma_{st} + 12.0\gamma_h\gamma_{st} + \Delta f_{pR}$$

$$= 10\frac{(202.5 \ ksi)(0.334 \ in.^2)}{105.75 \ in.^2}(1.07)(1.0) + 12(1.07)(1.0) + 2.4 \ ksi$$

$$= 22.08 \ ksi$$

Total loss: $\Delta f_{pT} = \Delta f_{pES} + \Delta f_{pLT} = 9.33 \ ksi + 22.08 \ ksi = 34.41 \ ksi$

Effective Stress: $f_{se} = f_{pi} - \Delta f_{pT} = 202.5\ ksi - 34.41\ ksi = 171.09\ ksi$

7.3 Flexural Capacity Calculation with Deck – Strain Compatibility Based on ACI 318-14 and PCI Design Handbook

Input data:

$f'_c = 7$ ksi

$f'_{ci} = 4$ ksi $\qquad\qquad\qquad\qquad$ l = 17.5 ft

$b_d = 9$ in. $\qquad\qquad\qquad\qquad$ $d_p = 25.125$ in.

$f_{pu} = 270$ ksi $\qquad\qquad\qquad\qquad$ $A_g = 146.24$ in.^{2}

$A_{ps} = 0.334$ in.^{2} $\qquad\qquad\qquad\qquad$ $I_g = 12529.68$ in.^{4}

$f_{se} = 171.09$ ksi $\qquad\qquad\qquad\qquad$ $y_b = 14.161$ in.

Require: $\qquad$ Flexural Strength (M_n)

Solution:

$A_s = 0.62$ in.^{2}; $A'_s = 1.24$ in.^{2}; d = 6.525 in.; d' = 2.525 in.

Assume c = 2.959 in.

$a = \beta . c = 0.7(2.959\ in.) = 2.072\ in.$

$E_{ci} = 3834.3\ ksi$

$n_i = 7.433$

99

$$A_{tr} = 146.24 \, in.^2 + (7.433 - 1)(0.334 \, in.^2) = 149.5 \, in.^2$$

$$y_{tr} = \frac{A_g y_b + A_{ps,tr} y_{ps}}{A_{tr}} = \frac{(146.24 \, in.^2)(14.161 \, in.) + (7.433 - 1)(0.334 \, in.^2)(2 \, in.)}{149.5 \, in.^2}$$

$$= 13.986 \, in.$$

$$I_{tr} = I_g + A_g d_g^2 + A_{ps,tr} d_{ps}^2$$

$$= 12529.68 \, in.^4 + (146.24.375 \, in.^2)(13.986 \, in. - 14.161 \, in.)^2$$

$$+ (7.906 - 1)(0.334 \, in.^2)(13.986 \, in. - 2.0 \, in.)^2 = 12842.86 \, in.^4$$

$$0.15 d_p = 0.15(25.125 \, in.) = 3.767 \, in. > d' = 2.525 \, in.$$

$$\therefore include \; compression \; steel \; in \; calculation$$

$$\varepsilon_s' = \frac{0.003}{c}(c - d') = \frac{0.003}{2.959 \, in.}(2.959 \, in. - 2.525 \, in.) = 0.00044$$

$$f_s' = \varepsilon_s' E_s = 0.00044(29{,}000 \, ksi) = 12.77 \, ksi$$

$$C = 0.85 f_c' b a + A_s' f_s' = 0.85(7 \, ksi)(9 \, in.)(2.072 \, in.) + 1.24 \, in.^2(12.77 \, ksi)$$

$$= 126.76 \, kips$$

$$\varepsilon_s = \frac{0.003}{c}(d - c) = \frac{0.003}{2.959 \, in.}(6.525 \, in. - 2.959 \, in.) = 0.0036 > 0.002 : f_s = f_y$$

$$\varepsilon_1 = \varepsilon_{se} = \frac{f_{se}}{E_p} = \frac{171.088 \, ksi}{28{,}500 \, ksi} = 0.006$$

$$P_e = A_{ps} f_{se} = 0.334 \, in.^2(171.088 \, ksi) = 57.14 \, kips$$

$$\varepsilon_2 = \left(\frac{P_e}{A_{tr}} + P_e \frac{e_{tr}^2}{I_{tr}}\right)\frac{1}{E_c} = \left(\frac{57.144 \, kips}{149.7 \, in.^2} + 57.144 \, kips \frac{11.973^2 \, in.^2}{12865.52 \, in.^4}\right)\frac{1}{4768.962 \, ksi}$$

$$= 0.000214$$

$$\varepsilon_3 = \varepsilon_t = \frac{0.003}{c}(d_p - c) = \frac{0.003}{2.959\ in.}(25.125\ in. - 2.959\ in.) = 0.0225$$

As $\varepsilon_t = 0.0225 > 0.005$, the classification is tension-controlled - $\phi = 0.9$.

$$\varepsilon_{ps} = \varepsilon_1 + \varepsilon_2 + \varepsilon_3 = 0.006 + 0.000214 + 0.0225 = 0.0287$$

$$\geq 0.0085\ (PCI\ Design\ Handbook)$$

$$f_{ps} = 270 - \frac{0.04}{\varepsilon_{ps} - 0.007} = 270 - \frac{0.04}{0.0287 - 0.007} = 268.16\ ksi$$

$$\varepsilon_{ty} = \frac{f_y}{E_s} = \frac{60\ ksi}{29,000\ ksi} = 0.00207$$

$$T = A_s f_s + A_{ps} f_{ps} = 0.62\ in.^2\ (60\ ksi) + 0.334\ in.^2\ (268.16\ ksi) = 126.764\ kips$$

As the total tension force is equal the total compression force, the assumed value of c is correct.

Moment about the neutral axis:

$$Mn = 0.85 f_c' b a \left(c - \frac{a}{2}\right) + A_s' f_s' (c - d') + A_s f_y (d - c) + A_{ps} f_{ps} (d_p - c)$$

$$= 0.85(7\ ksi)(9\ in.)(2.072\ in.)\left(2.959\ in. - \frac{2.072\ in.}{2}\right)$$

$$+ 1.24 in.^2\ (12.769\ ksi)(2.959\ in. - 2.525\ in.)$$

$$+ 0.62 in.^2\ (60\ ksi)(6.525\ in. - 2.959\ in.)$$

$$+ 0.334\ in.^2\ (268.16\ ksi)(25.125\ in. - 2.959\ in.) = 2338.147 k. in$$

$$= 194.85\ k.ft$$

Based on strain compatibility method, the point load that causes moment failure is 68.73 kips. However, the f_{ps} above was calculated based on assumption of the loading point located

outside of the development length. As the development length was in consideration, the f_{ps} would change. The development length of prestressed girder, which includes of the transfer length and flexural bond length, was calculated following ACI 318-14 section R25.4.8.3.

$$l_d = \left(\frac{f_{se}}{3000}\right) \cdot d_b + \left(\frac{f_{ps} - f_{se}}{1000}\right) \cdot d_b$$

The transfer length of the prestressed girder was calculated:

$$\left(\frac{f_{se}}{3000}\right) \cdot d_b = \left(\frac{171.09 \; ksi}{3000}\right)(0.52 \; in.) = 29.66 \; in.$$

The flexural bond length the prestressed girder was calculated:

$$\left(\frac{f_{ps} - f_{se}}{1000}\right) \cdot d_b = \frac{(268.16 \; ksi - 171.09 \; ksi)}{1000}(0.52 \; in.) = 50.47 \; in.$$

Distance of loading point from the initial prestress transfer $= 3.5 \; ft \left(12 \frac{in.}{ft}\right) -$ $18 \; in. \; (the \; corroded \; region) = 24 \; in.$ The development length is the sum of the transfer length and the flexural bond length, which is 80.13 in. Therefore, the moment capacity at the cross section in the development length should be reduced because the prestressing steel in in this region was not fully developed to achieve its maximum stress. The span between the point load and the center of the support is $l = 3.25 \; ft.$

So,

$$M = \frac{Pab}{l} + \frac{wx}{2}(l - x) \rightarrow P = \left(M - \frac{wx}{2}(l - x)\right)\frac{l}{ab}$$

$$= \left(194.85 \; k.ft - \frac{0.15\frac{k}{ft}(3.5 \; ft)}{2}(17.5 \; ft - 3.25 \; ft)\right)\frac{17.5 \; ft}{3.25 \; ft \; (14.25 \; ft)}$$

$$= 72.3 \; kips$$

$$R = P.\frac{l - x}{L} + \frac{wl}{2} = \; kips \; \frac{17.5 \; ft - 3.25 \; ft}{17.5 \; ft} + \frac{0.15\frac{k}{ft}(17.5 \; ft)}{2} = 60.2 \; kips$$

However, because of the simulated damage in the corroded region, the flexural capacity in range of the corroded region where prestressing strands did not bond to concrete, shall be computed as the flexural capacity of reinforced concrete instead of prestressed concrete. The flexural capacity calculation of reinforced concrete is performed below.

Assume c = 2.528 in.

$$a = \beta_1 c = 0.7(2.528 \; in.) = 1.77 \; in.$$

$$\varepsilon_s' = \frac{0.003}{c}(d' - c) = \frac{0.003}{2.528 \; in.}(2.525 \; in. -2.528 \; in.) = -0.0000038 < 0.00207$$

$$\varepsilon_s = \frac{0.003}{c}(d - c) = \frac{0.003}{2.528 \; in.}(6.525 \; in. -2.528 \; in.) = 0.00474 < 0.005$$

$$\varepsilon_p = \frac{0.003}{c}(d_p - c) = \frac{0.003}{2.528 \; in.}(25.125 \; in. -2.528 \; in.) = 0.0268$$

$$f_{ps} = 270 - \frac{0.04}{\varepsilon_{ps} - 0.007} = 270 - \frac{0.04}{0.0268 - 0.007} = 267.98 \; ksi$$

103

In the discontinuity region, there is no transfer length due to no prestressing force was transferred in this region, except flexure bond length, which was bonding to the repair material and acting like tension reinforcement.

The new flexural bond length the prestressed girder was calculated:

$$\left(\frac{f_{ps}}{1000}\right) \cdot d_b = \frac{268.16 \; ksi}{1000} (0.52 \; in.) = 139.44 \; in.$$

$$f_{ps,reduced} = 267.98 \; ksi \frac{15 \; in.}{139.44 \; in} = 28.83 \; ksi$$

$$C = 0.85 f_c' ba + A_s' f_s' = 0.85(7 \; ksi)(9 \; in.)(1.77 \; in.) + 1.24 \; in.^2 (0.0000038)(29{,}000 \; ksi)$$

$$= 94.9 \; kips$$

$$T = A_s f_s + A_{ps} f_{ps,reduced} = 0.62 \; in.^2 (29{,}000 \; ksi)(0.00474) + 0.334 \; in^2 (22.83 \; ksi)$$

$$= 94.9 \; kips$$

As the total tension force is equal to the total compression force, the assumed value of c is correct.

Moment about the neutral axis:

$$Mn = 0.85 f_c' ba \left(c - \frac{a}{2}\right) + A_s' f_s' (d' - c) + A_s f_y (d - c) + A_{ps} f_{py} (d_p - c)$$

$$= 0.85(7 \; ksi)(9 \; in.)(1.77 \; in.) \left(2.528 \; in. - \frac{1.77 \; in.}{2}\right)$$

$$+ 1.24 \; in.^2 (-0.0000038)(29{,}000 \; ksi)(2.525 \; in. - 2.528 \; in.)$$

$$+ 0.62 \; in.^2 (29{,}000 \; ksi)(0.00474)(6.525 \; in. - 2.528 \; in.)$$

$$+ 0.334 \; in^2 (22.83 \; ksi)(25.125 \; in. - 2.528 \; in.) = 714.13 \; k.in = 59.51 \; k - ft$$

The effective length of this region, which is from the center of the support to the end of discontinuity region, is 1.25 ft.

$$M = \frac{Pbx}{l} + \frac{wx}{2}(l-x) \rightarrow P = \left(M - \frac{wx}{2}(l-x)\right)\frac{l}{bx}$$

$$= \left(59.51\ k.ft \right.$$

$$\left. -\frac{0.15\frac{k}{ft}(1.25\ ft)}{2}(17.5\ ft - 1.25\ ft)\right)\frac{17.5\ ft}{1.25\ ft\ (17.5\ ft - 3.25\ ft)}$$

$$= 57\ kips$$

$$R = P.\frac{l-x}{L} + \frac{wl}{2} = 57\ kips\ \frac{17.5\ ft - 1.25\ ft}{17.5\ ft} + \frac{0.15\frac{k}{ft}(17.5\ ft)}{2} = 54\ kips$$

Therefore, the load for maximum concentrated load to reach the calculated flexural strength is in the range between 57 kips and 72.3 kips. The difference comes from the difference between reinforced concrete and prestressed concrete behavior.

7.4 Shear Capacity Calculation Based on AASHTO LRFD General Method

The purpose of this calculation is to determine the shear capacity of the girder and required shear steel at multiple locations along the girder as well as the location of the point load (3.5 ft from the end of the girder). A spreadsheet was developed using AASHTO LRFD (2017) General Method, which assisted to find the load and the location causing shear failure of the end region. The calculation is shown below following step-by-step.

Input data:

$A_{ps} = 0.334$ in.^{2} $L = 18$ ft

$d_p = 25.125$ in. $A_v = 0.22$ in.^{2}

$E_p = 28,500$ ksi $w_0 = 0.15$ k/ft

$f_{pu} = 270$ ksi $f_y = 60$ ksi

$f_{py} = 243$ ksi $E_s = 29,000$ ksi

$f_{pi} = f_j = 202.5$ ksi $f'_s = 12.769$ ksi

$A_s = 0.62$ in.^{2} $h = 27.125$ in.

$A'_s = 1.24$ in.^{2} $\alpha = 0.85$ (f'$_c \leq 10$ ksi)

$f'_c = 7$ ksi $\beta_1 = 0.7$ (f'$_c = 7$ ksi)

$f'_{ci} = 4$ ksi $a = 2.072$ in.

$b_d = 9$ in. $f_{ps} = 268.16$ ksi

$x = 3.5$ ft

$c = 2.959$ in. (From strain compatibility calculation in Section 7.3)

Require: Calculate shear capacity x = 3.5 ft using AASHTO General Method.

Solution:

a) Determine d_v

$$k = 2 \cdot \left(1.04 - \frac{f_{py}}{f_{pu}}\right) = 2\left(1.04 - \frac{243 \ ksi}{270 \ ksi}\right) = 0.28$$

$$d_e = \frac{A_{ps}f_{ps}d_p + A_s f_y d_s}{A_{ps}f_{ps} + A_s f_y}$$

$$= \frac{0.334\ in.^2\ (268.16\ ksi)(25.125\ in.) + 0.62\ in.^2\ (60\ ksi)(6.525\ in.)}{0.334\ in.^2\ (268.16\ ksi) + 0.62\ in.^2\ (60\ ksi)}$$

$$= 19.67\ in.$$

$$d_{v1} = 0.9d_e = 0.9(19.67\ in.) = 17.7\ in.$$

$$d_{v2} = 0.72h = 0.72(27.125\ in.) = 19.53\ in.$$

The maximum value between d_{v1} and d_{v2} is chosen. So, the $d_v = 19.53$ in.

$$w_u = w_0 = 0.15\frac{k}{ft}$$

b) At the support

The minimum of the concentrated load of 57 kips calculated in Section 7.3 is used to computed V_u.

$$V_u = \frac{w_u l}{2} + \frac{Pb}{l} = \frac{0.15\frac{k}{ft}(17.5\ ft)}{2} + \frac{57\ kips(17.5\ ft - 3.25\ ft)}{17.5\ ft} = 47.73\ kips$$

$$M_u = 0$$

c) At x = 3.25 ft from the center of the support

$$V_u(x) = V_u - x \cdot w_u = 47.73\ kips - 3.25ft\left(0.15\frac{k}{ft}\right) = 47.24\ kips$$

$$M_u = \frac{1}{2}(V_u + V_u(x)) \cdot x = \frac{1}{2}(47.73\ kips + 47.24\ kips)(3.25\ ft) = 166.2\ k - ft$$

$$\varepsilon_s = \frac{\dfrac{|M_u|}{d_v} + 0.5N_u + |V_u - V_p| - A_{ps}f_{po}}{E_sA_s + E_pA_{ps}}$$

$$= \frac{\dfrac{\left|166.2\ k - ft\left(12\ \frac{in.}{ft}\right)\right|}{19.53\ in.} + 0.5(0) + |47.24\ kips - 0| - 0.334\ in^2(0.7)(270\ ksi)}{0.62\ in^2(29{,}000\ ksi) + 0.334\ in^2(28{,}500\ ksi)}$$

$$= 0.00314$$

$$\beta = \frac{4.8}{1 + 750\varepsilon_s} = \frac{4.8}{1 + 750(0.00314)} = 1.432$$

$$V_C = 0.0316\beta\sqrt{f_c'}\lambda b_v d_v = 0.0316(1.432)\sqrt{7\ ksi}(1.0)(3\ in.)(19.53\ in.) = 7.02\ kips$$

$$v_u = \frac{|V_u - \emptyset V_p|}{\emptyset b_v d_v} = \frac{|47.24\ kips - 0|}{0.85(3\ in.)(19.53\ in.)} = 0.949\ ksi \ge 0.125f_c' = 0.125(7\ ksi)$$

$$= 0.875\ ksi$$

So, $s_{max} = 0.4d_v = 0.8(19.53\ in.) = 7.8\ in. \le 12.0\ in.$

Therefore, use double No.3 stirrups for all shear reinforcement shear following Figure 3.2.

Spacing of the stirrup under point load is s = 4 in.

$$V_s = \frac{A_v f_y d_v (cot\theta + cot\alpha)sin\alpha}{s}$$

   Where:

   $\alpha = 90°$, for vertical shear reinforcement

   $\theta = 29 + 3500\varepsilon_s = 29 + 3500(0.00314) = 39.37°$

   $$V_s = \frac{A_v f_y d_v cot\theta}{s} = \frac{0.22\ in^2(60\ ksi)(19.53\ in.)(cot\ 39.37°)}{4\ in.} = 76.88\ kips$$

108

$$V_n = V_c + V_s = 7.02\ kips + 76.88\ kips = 89.9\ kips$$

$$or\ V_n = 0.25f_c'd_vb_v = 0.25(7\ ksi)(19.53\ in.)(3\ in.) = 102.53\ kips$$

The shear capacity is the minimum of two values of V_n. Therefore,

$$V_n\ (capacity) = 89.9\ kips$$

$$V\ (based\ on\ P = 57\ kips\ at\ 3.5\ ft\ from\ the\ end\ of\ girder) = 47.24\ kips$$

However, the effect of transfer length should be accounted into the calculation, which would make the shear capacity decreasing as the applied load was located in range of transfer length.

$$\varepsilon_s = \frac{\frac{|M_u|}{d_v} + 0.5N_u + |V_u - V_p| - A_{ps}f_{po}}{E_sA_s + E_pA_{ps}}$$

$$= \frac{\frac{\left|166.2\ k.ft(12\frac{in.}{ft}\right|}{19.53\ in.} + 0.5(0) + |47.24\ kips - 0| - 0.334\ in^2(0.7)(270\ ksi)\frac{(3.5\ ft - 1.5\ ft)\left(12\frac{in.}{ft}\right)}{29.66}}{0.62\ in^2(60,000\ ksi) + 0.334\ in^2(28,500\ ksi)}$$

$$= 0.00357$$

$$\beta = \frac{4.8}{1 + 750\varepsilon_s} = \frac{4.8}{1 + 750(0.00357)} = 1.304$$

$$V_C = 0.0316\beta\sqrt{f_c'}\lambda b_vd_v = 0.0316(1.304)\sqrt{7\ ksi}(1.0)(3\ in.)(19.53\ in.) = 6.39\ kips$$

$$\theta = 29 + 3500\varepsilon_s = 29 + 3500(0.00357) = 41.51°$$

$$V_s = \frac{A_vf_yd_v\cot\theta}{s} = \frac{0.22\ in^2(60\ ksi)(19.53\ in.)(\cot 41.51°)}{4\ in.} = 72.83\ kips$$

$$V_n = V_c + V_s = 6.39\ kips + 72.83\ kips = 79.22\ kips < 0.25f_c'd_vb_v = 102.53\ kips$$

So, $V_{n,reduced}$ $(capacity) = 79.22\ kips.$ Based on the results above, the applied load of 57 kips that generated the shear force of 47.24 kips and the moment of 166.2 k-ft. However, as compared to the moment of 194.85 k-ft from the flexural capacity, the support reaction could be greater than 47.24 kips to cause flexural failure. In addition, the applied load was lesser than the reduced shear capacity of 79.22 kips at the loading point, so the applied load could not cause shear failure and flexure. However, as compared to non-prestressed region, the moment caused by the applied load, 166.2 k-ft, was larger than beam's flexural capacity, 59.51 k-ft. Therefore, flexural failure would occur in the non-prestressed region.